LAWRENCE
LIVERMORE
NATIONAL
LABORATORY

UCRL-PROC-225433

High-Performance Corrosion-Resistant Iron-Based Amorphous Metals - The Effects of Composition, Structure and Environment: $Fe_{49.7}Cr_{17.7}Mn_{1.9}Mo_{7.4}W_{1.6}B_{15.2}C_{3.8}Si_{2.4}$

J. Farmer, J. Haslam, S. Day, T. Lian, C. Saw, P. Hailey, J-S. Choi, N. Yang, R. Bayles, L. Aprigliano, J. Payer, J. Perepezko, K. Hildal, E. Lavernia, L. Ajdelsztajn, D. J. Branagan, M. B. Beardsely

October 20, 2006

2006 MRS Fall Meeting
Boston, MA, United States
November 28, 2006 through December 1, 2006

Disclaimer

HIGH-PERFORMANCE CORROSION-RESISTANT IRON-BASED AMORPHOUS METALS – THE EFFECTS OF COMPOSITION, STRUCTURE AND ENVIRONMENT: $Fe_{49.7}Cr_{17.7}Mn_{1.9}Mo_{7.4}W_{1.6}B_{15.2}C_{3.8}Si_{2.4}$

J. Farmer[1], J. Haslam[1], S. Day[1], T. Lian[1], C. Saw[1], P. Hailey[1], J-S. Choi[1], N. Yang[2], R. Bayles[3], L. Aprigliano[4], J. Payer[5], J. Perepezko[6], K. Hildal[6], E. Lavernia[7], L. Ajdelsztajn[7], D. J. Branagan[8] and M. B. Beardsely[9]

[1]Lawrence Livermore National Laboratory, [2]Sandia National Laboratory, [3]Naval Research Laboratory, [4]Strategic Analysis, [5]Case Western Reserve University, [6]University of Wisconsin Madison, [7]University of California Davis, [8]The NanoSteel Company and [9]Caterpillar

ABSTRACT

Several Fe-based amorphous metal formulations have been identified that appear to have corrosion resistance comparable to (or better than) that of Ni-based Alloy C-22 (UNS # N06022), based on measurements of breakdown potential and corrosion rate in seawater. Both chromium (Cr) and molybdenum (Mo) provide corrosion resistance, boron (B) enables glass formation, and rare earths such as yttrium (Y) lower critical cooling rate (CCR). SAM2X5 ($Fe_{49.7}Cr_{17.7}Mn_{1.9}Mo_{7.4}W_{1.6}B_{15.2}C_{3.8}Si_{2.4}$) has no yttrium, and is characterized by relatively high critical cooling rates of approximately 600 Kelvin per second. Data for the SAM2X5 formulation is reported here. In contrast to yttrium-containing iron-based amorphous metals, SAM2X5 can be readily gas atomized to produce spherical powders which enable more facile thermal spray deposition.

The reference material, nickel-based Alloy C-22, is an outstanding corrosion-resistant engineering material. Even so, crevice corrosion has been observed with C-22 in hot sodium chloride environments without buffer or inhibitor. SAM2X5 also experiences crevice corrosion under sufficiently harsh conditions. Both Alloy C-22 and Type 316L stainless lose their resistance to corrosion during thermal spraying, due to the formation of deleterious intermetallic phases which depletes the matrix of key alloy elements, whereas SAM2X5 can be applied as coatings with the same corrosion resistance as a fully-dense completely amorphous melt-spun ribbon, provided that its amorphous nature is preserved during thermal spraying.

The hardness of Type 316L Stainless Steel is approximately 150 VHN, that of Alloy C-22 is approximately 250 VHN, and that of HVOF SAM2X5 ranges from 1100-1300 VHN [MRS12-13]. Such hardness makes these materials particularly attractive for applications where corrosion-erosion and wear are also issues. Since SAM2X5 has high boron content, it can absorb neutrons efficiently, and may therefore find useful applications as a criticality control material within the nuclear industry.

INTRODUCTION

This research has two primary long-term goals, all directed towards development of advanced amorphous-metal thermal-spray coatings with corrosion resistance superior to Type 316L stainless steel [UNS # S31603] and nickel-based Alloy C-22 [UNS # N06022]. Computational materials science has been used to help guide the design these new materials.

Novel Fe-Based Amorphous Metal Coatings

Several Fe-based amorphous metal formulations have been found that appear to have corrosion resistance comparable to, or better than that of Ni-based Alloy C-22, based on breakdown potential and corrosion rate [1-3]. These formulations use chromium (Cr), molybdenum (Mo), and tungsten (W) to provide corrosion resistance, boron (B) to enable glass formation, and yttrium to lower the critical cooling rate (CRR). SAM1651 ($Fe_{48.0}Cr_{15.0}Mo_{14.0}B_{6.0}C_{15.0}Y_{2.0}$) has yttrium added [4-6], and has a nominal critical cooling rate of only 80 Kelvin per second, while SAM2X5 ($Fe_{49.7}Cr_{17.7}Mn_{1.9}Mo_{7.4}W_{1.6}B_{15.2}C_{3.8}Si_{2.4}$) has no yttrium, and is characterized by relatively high critical cooling rates of approximately 600 Kelvin per second. Note that SAM1651 is also known as SAM7. Corrosion data for the SAM2X5 formulation, which is based upon a master alloy known as either SAM40 or DAR40 [7-12] is reported here.

SAM1651 has a low critical cooling rate (CCR), due to the addition of yttrium (Y), which enables it to be rendered as a completely amorphous thermal spray coating. Unfortunately, it is relatively difficult to atomize, with powders being irregular in shape. This causes the powder to be difficult to pneumatically convey during thermal spray deposition. Gas atomized SAM1651 powder has required exotic milling techniques to eliminate irregularities that make flow difficult. SAM2X5 (no yttrium) has a high critical cooling rate, which has caused problems associated with devitrification. However, in contrast to SAM1651, SAM2X5, and the master alloy used for its preparation, can be readily gas atomized to produce spherical powders which enable more facile thermal spray deposition.

Protective coatings of nickel-based Alloy C-22 and Type 316L stainless can be applied with thermal spray technology [13]. However, their corrosion resistance is lost at the high temperatures required for deposition [1-3]. Based upon extensive studies of these austenitic alloys in wrought form, it is believed that this loss in corrosion resistance may be due to the precipitation of undesirable phases (P, σ, and μ). These precipitated phases deplete the matrix of those alloying elements responsible for passivity. In contrast, SAM2X5 and SAM1651 coatings can be applied with thermal spray processes without any significant loss of corrosion resistance.

It is important to point out that the outstanding corrosion possible with amorphous metals has been recognized for many years [14-16]. A number of other iron-based amorphous metals have been published, including several with very good corrosion resistance. Examples include: thermally sprayed coatings of Fe-10Cr-10-Mo-(C,B) which were explored as early as 1996 by Kishitake et al. [17]; bulk Fe-Cr-Mo-C-B [18]; and Fe-Cr-Mo-C-B-P [19]. The corrosion resistance of the Fe-Cr-Mo-C-B-P alloy [18] was corroborated by these authors [1-3]. Nickel-based materials have also been developed which exhibit exceptional corrosion performance [20].

Other Attributes of Fe-Based Amorphous Metal Coatings

Such materials are extremely hard, and provide enhanced resistance to abrasion and gouges (stress risers) from backfill operations, and possibly even tunnel boring. The hardness of Type 316L Stainless Steel is approximately 150 VHN, that of Alloy C-22 is approximately 250 VHN, and that of HVOF SAM2X5 ranges from 1100-1300 VHN [7]. SAM2X5 and SAM1651 coatings can be applied with thermal spray processes without any significant loss of corrosion resistance.

Both SAM2X5 & SAM1651 have high boron content which should enable them to absorb neutrons and therefore be used for criticality control in baskets. Alloy C-22 and 316L have no neutron absorber, and cannot be used for such functions. Borated stainless steel and Gd-doped Ni-Cr-Mo alloys are being developed but may face limitations related to their availability, cost, corrosion and leach resistance, and mechanical properties. Tests with J-13 well waters have shown that boron can preferentially leach boron, the neutron absorber, from borated stainless steels. Well J-13 water has a typical water chemistry for saturated zone and perched waters at Yucca Mountain and a mean composition that was reported by Harrar et al. [21]. During evaporation of J-13 water, Na^+, K^+, Cl^-, and NO_3^- are concentrated, and HCO_3^-, Ca^{2+} and Mg^{2+} can be removed from solution by the precipitation of calcium and magnesium carbonate.

Importance of Chromium, Molybdenum and Tungsten

The importance of chromium, molybdenum and tungsten additions to amorphous metals as a means of enhancing corrosion resistance is discussed in this section. The decision to achieve enhanced corrosion resistance in these Fe-based amorphous metals was initially based upon two considerations. First, substantial enhancements in corrosion resistance had been observed in stainless steels and nickel based alloys by adding molybdenum, as well as other alloying elements. Secondly, this enhancement in localized corrosion resistance can be quantified in the pitting resistance equivalence number, and could be used as a guide to determine the level of molybdenum addition necessary to achieve localized corrosion resistance comparable to nickel-based Alloy C-22, one of the benchmark materials. Branagan has used estimates of PREN to determine the maximum molybdenum additions to the series of melt-spun ribbons which include SAM2X1, SAM2X3, SAM2X5 and SAM2X7. Based upon these calculations, it was believed that the new SAM2X5 and SAM2X7 compositions possessed enough molybdenum to demonstrated passive film stability comparable to nickel-based Alloy C-22. This hypothesis has been tested in this investigation, and found to have merit.

The importance of molybdenum in nickel-based alloys has been recognized for many years. Alloy C-22 (UNS N06022) is now being considered for construction of the outer barrier of the WP. This alloy consists of 20.0-22.5% Cr, 12.5-14.5% Mo, 2.0-6.0% Fe, 2.5-3.5% W, 2.5% (max.) C, and balance Ni. Alloy C-22 is less susceptible to localized corrosion in environments that contain Cl^- than Alloys 825 and 625, materials of choice in earlier designs. The unusual localized corrosion resistance of Alloy C-22 is apparently due to the additions of Mo and W, both of which are believed to stabilize the passive film at very low pH [22]. The oxides of these elements are very insoluble at low pH. Consequently, Alloy 22 exhibits relatively high thresholds for localized attack. High repassivation potentials have been observed by some [23], while others have found very low corrosion rates in simulated crevice solutions containing 10 wt. % $FeCl_3$ [24].

EXPERIMENTAL PROCEDURES

Nomenclature for Alloy Designation

In early reports and publications on the development of these Fe-based amorphous metals [1-12], the SAM40 master alloy carried the designation DAR40, the SAM-series alloys were know as the LDAR-series alloys, and the SAM1651 alloy carried either CBCLT or CBCTL prefixes. The "DAR" prefix was used to acknowledge sponsorship of the research program by the Defense Advanced Research Projects Agency, DARPA [7-12]. The "LDAR" prefix was used to acknowledge modifications of the original DAR-type alloys, under sponsorship of the DOE-DARPA High Performance Corrosion Resistant Materials Program, HPCRM Program, at Lawrence Livermore National Laboratory [1-3]. The "CBCTL" and "CBCLT" are the initials of those who prepared SAM1651 ingots for the HPCRM Program (C. Blue and C. T. Liu). The "SAM" prefix has been used to begin developing a unified designation for these Fe-based amorphous metals, and acknowledges the DARPA Structural Amorphous Metals (SAM) program that funded early development the DAR, LDAR, and CBCTL/CBCLT alloys.

Melt Spinning Process

The development of an appropriate powder composition for the production of a corrosion-resistant thermal-spray coating requires that the alloy first be tested in a form with no porosity, and with little or no crystalline phases present. Testing of such materials enables determination of the best possible corrosion performance for a given composition. Melt spinning and arc-melting with drop casting have been used as methods to synthesize completely amorphous, Fe-based, corrosion-resistant alloys with near theoretical density, thereby enabling the effects of coating morphology on corrosion resistance to be separated from the effects of elemental composition.

Cooling rates approaching one billion Kelvin per second (10^9 K/s) may be achieved with physical vapor deposition (PVD), and can be used to produce amorphous metal thin films. However, other processes are required to produce free-standing materials and coatings of practical thickness for corrosion and wear resistance. The thickness of PVD films is typically one to five microns (1-5 μm). Maximum cooling rates of one million Kelvin per second (10^6 K/s) have been achieved with melt spinning, and is therefore ideal for producing amorphous metals over a very broad range of compositions. The melt-spun ribbon (MSR) samples produced with this equipment are several meters long, several millimeters wide and approximately 150 microns thick [7]. In contrast, the cooling rate in a typical thermal spray process such as HVOF are on the order of ten thousand Kelvin per second (10^4 K/s). The compositional range of materials that can be rendered as amorphous metals with thermal spray is therefore more restricted.

The melt spinning involves the ejection of a liquid melt onto a rapidly moving copper wheel with a pressure-controlled gas. The liquid melt solidifies onto the wheel, with subsequent separation from the wheel by thermal contraction and centrifugal force, and collection in a chamber. By changing the tangential velocity of the wheel, as well as other processing parameters, the cooling rate can be controlled over a very broad range. The specific processing parameters for the melt-spinning process can be selected to establish cooling rates that are representative of a given thermal spray process. If a specific cooling rate produces an amorphous, glassy metal during melt spinning, it should also produce a glassy structure during thermal spray. It is therefore

possible to use melt spinning to simulate the type of microstructure that can be achievable with thermal spraying, such as the high-velocity oxy-fuel process. Furthermore, an entire series of developmental materials, with different compositions, heat capacities, and thermal conductivity, can be made with the same cooling rates, so that the ease of processing each can be compared.

By exploiting the melt spinning process, several alloy compositions of Fe-based amorphous metals have been produced, characterized, and tested [1-3]. Several of these were compositional modifications of the SAM40 master alloy [7-12], and were prepared by following the general formula: $[(SAM40)_{100-x} + Z_x]$ where Z is the added element, and x is the amount of the addition in atomic percent [7]. Additives investigated included nickel, chromium, molybdenum, tungsten, yttrium, titanium and zirconium. The nickel and molybdenum additions are known to greatly influence the electrochemical properties of conventional stainless steel alloys. The yttrium, titanium, and zirconium additions, while not normally added to steels are known to form very stable oxides and are expected to increase the stability and passivity of the oxide film in a variety of environments. The SAM1651 formulation has the same nominal elemental composition as the Y-containing Fe-based amorphous metal formulation discussed in the literature [4-6]. These rare-earth containing materials have been selected with particular emphasis on glass forming ability, thermal stability, hardness, and corrosion resistance, all under conditions of interest.

The melt-spinning process was used to perform a systematic study of various elemental compositions, each based on the Fe-based SAM40 master alloy, with 1, 3, 5, and 7 atomic percent additions of specific elements believed to be beneficial to glass formation or corrosion resistance. The alloy compositions explored during this study are summarized in Tables 1 and 2. Elemental additions investigated included nickel, molybdenum, yttrium, titanium, zirconium, and chromium. The densities of the amorphous metals prepared with melt spinning were determined, and all were less dense than nickel-based N06022 (Alloy C-22), and therefore offer a weight advantage over such classical corrosion-resistant alloys. The first re-crystallization peak for each of melt-spun ribbons was determined with differential thermal analysis (DTA), and was similar to that of the master alloy (SAM40). The formula with the yttrium additions showed re-crystallization peaks at higher temperatures than achieved with other formulae, corroborating the fact that yttrium additions do indeed promote thermal stability and glass formability. Some formulae exhibited a second re-crystallization process at a higher temperature than the first, with titanium and zirconium based formulations showing these processes at the highest temperatures. All of the "as-cast" amorphous metal formulae produced by the HPCRM Team exhibited hardness far superior to many of the conventional materials of interest, such as Type 316L stainless steel, and nickel-based N06022 (Alloy C-22). Thus, coatings of these materials would also be expected to be less prone to erosion, wear and gouging than conventional engineering alloys. Partially de-vitrified samples of the HPCRM materials exhibited dramatic increases in hardness. Thus, carefully controlled heat treatment of these materials can be used to achieve dramatic improvements in resistance to erosion, wear and penetration.

Thermal Spray Process

Several thermal spray processes have been developed by industry and include: flame spray, wire-arc; plasma spray; water-stabilized plasma spray; high-velocity oxy-fuel; and the detonation gun. Any of these can be used for the deposition of Fe-based amorphous metals, with varying degrees of residual porosity and crystalline structure. The coatings discussed here were made with the

high-velocity oxy-fuel (HVOF) process, which involves a combustion flame, and is characterized by gas and particle velocities that are three to four times the speed of sound (mach 3 to 4). This process is ideal for depositing metal and cermet coatings, which have typical bond strengths of 5,000 to 10,000 pounds per square inch (5-10 ksi), porosities of less than one percent (< 1%) and extreme hardness.

Optimization of the thermal spray process through careful selection of powder size and process temperature, has now yielded coatings of SAM40 (non-optimized elemental coating) that are virtually pore-free, and for all practical purposes, fully dense. These new coating architectures have also been shown, through detailed examination with X-ray diffraction (XRD) and scanning electron microscopy (SEM), to be amorphous. An optimized thermal spray process is now being used to render SAM2X5 and SAM1651 amorphous metal formulations as high-performance corrosion-resistant coatings, with nearly full density, no significant porosity, and good bond strength.

Energy Dispersive Analysis with X-Rays – Composition

Electron microanalysis of melt-spun ribbons was performed on a series of Fe-based formulations and on Alloy C-22 and Type 316L stainless reference materials. Scanning electron microscopy (SEM) was used to image superficial microstructure using both secondary and backscattered electron detectors. Semi-quantitative elemental composition of the melt-spun ribbons was determined with energy-dispersive X-ray spectroscopy (EDS, EDAX).

Segments of each ribbon were imaged using a Quanta Series 200 environmental scanning electron microscope (ESEM). Images were obtained from both sides of the ribbon, using both secondary electron and back-scattered electron detectors. The side of each ribbon that had been in contact with the melt-spinning copper wheel was distinguishable as being noticeably rougher than the non-contact side.

Semi-quantitative elemental composition was determined with EDS. Compositional analysis was performed on the smoother side of each ribbon, as the rougher sides were found in some cases to be contaminated with small amounts of copper, presumably from contact with the copper wheel during the melt spinning process. Quantification of the light elements, such as boron (B) and carbon (C), was found to be unreliable for these complex sample formulations. The given (formulation) values for these elements were therefore assumed and used in calculating the compositional values for the remaining heavier elements. Microanalysis of each sample was performed at three randomly-selected locations at 10,000X magnification, with the average being reported here.

X-Ray Diffraction – Crystal Structure

The basic theory of X-ray diffraction of amorphous materials is well developed and has been published in the literature [25, 26]. A brief summary is presented here to place experimental data for the Fe-based amorphous metals in proper perspective. For crystalline diffraction, specific x-ray peaks can be observed from a diffraction pattern acquired from x-ray diffractometer for crystalline materials. These peaks are the results of constructive interference of the probing X-ray wave. If the sample is single crystal, these peaks have specific arrangements and orientations. The positions and intensities of these peaks are related to the atomic arrangements in the unit cell

of the crystals. Unit cells have 3 axes with 3 angles (called lattice parameters), and they can be grouped into triclinic, monoclinic, orthorhombic, tetragonal, hexagonal, rhombohedral or cubic structures. In general, specific compounds have specific lattice parameters and the compounds can be identified by these parameters. The lattice parameters consist of three axes and three angles.

In an amorphous material, the atoms are not arranged in a periodic fashion such that crystals can be formed. There are broad diffraction peaks, which belong to the amorphous structure. The amorphous state does have structure as defined by the radial distribution function and the partial radial distribution, if it is a multiple elements system. For the present effort, such an analysis is not necessary at the moment. The degree of crystalline structure is correlated to the intensity of each scattering component.

The X-ray diffraction experiment is carried out using the Philip vertical goniometer in the para-focusing or also known as the Bragg-Bretano method. The X-ray optics are self-focusing, and the distance between the X-ray focal point to the sample position is equal to the distance between the sample position and the receiving slit for the reflection mode. Thus, the intensity and resolution are optimized. Parallel vertical slits are also added to improve the scattering signal.

Scintillation detectors are used in most modern X-ray diffractometers. However, the energy resolution is not sufficient to discriminate fluorescence X-rays of certain elements with energy close to the probing X-ray energy. Hence, very often, an analyzing crystal is used after the receiving slit. The choice of the crystal is based on the crystal mosaic, for energy selectivity and the efficiency. The most widely use energy discriminator is usually graphite for efficiency without significantly scarifying X-ray intensity. This is particularly important for the HPCRM because of the iron content in the samples. Iron fluorescence has energy which is close to that of the copper K_α probing X-ray. Sometime X-ray filters are used.

In the present setup, CuK_α is used with a graphite analyzing crystal. Step scan is performed from 20 to 90° (2θ) with step size of 0.02° at 4-10 seconds per point, depending on the amount of sample. The samples are loaded onto low quartz holders. This is because the expected intensity is very low and hence background scattering needs to be minimized.

Thermal Properties

The thermal properties of these Fe-based amorphous metals have been determined by Perepezko and Hildal. Thermal analysis of these Fe-based amorphous metals, with differential scanning calorimetry (DSC) or differential thermal analysis (DTA), allows determination of important thermal properties such as the glass transition temperature T_g, crystallization temperature T_x and melting interval T_m-T_L. Results from the thermal analysis of amorphous samples provides initial assessment of the glass forming ability of these samples through conventional metrics such as T_{rg} (T_g/T_L), T_x ($=T_x-T_g$) and γ ($=T_x/(T_g+T_L)$ that can be used to rank alloys based on the expected suitability for thermal spray processing. However, note that the metrics provided by thermal analysis are only initial assessments, and more detailed studies are required to determine the glass formability of a particular alloy. These data are summarized in Table 3.

Perepezko and his colleagues have also used wedge casting allows accurate determination the cooling rate required to avoid crystallization of the melt upon continuous cooling. A continuous range of cooling rates can be experienced simultaneously by an amorphous metal formulation by casting into a wedge-shaped mold for solidification. Then, examination of the wedge-shaped ingot's microstructure as a function of position reveals the lowest possible cooling rate (correlated with position) that can be used to maintain the material in a glassy state. The cooling rates in the wedge can be predicted with finite element modeling, and can be determined experimental with optical pyrometers (or other comparable methods).

In order to use amorphous coatings in application such as nuclear waste storage, it is crucial to determine the long-term stability of the amorphous phase, as precipitation of crystalline phases such as bcc-Fe will severely reduce the overall corrosion resistance of the coating. A convenient way to visualize thermal stability is the calculation of Time-Temperature-Transformation (TTT) curves that consists of the loci of time-temperature for the onset of nucleation of crystalline phases occurs. A kinetic model as been developed that combines information from wedge casting experiments and isothermal annealing experiments and incorporates these into a heterogeneous nucleation model. Based on this model, TTT-diagrams have been assessed for alloys SAM35 and SAM40, whereas work is in progress (preliminary results are available) for determining the TTT-curves for SAM2X5 and other alloys of interest.

Mechanical Properties

Hardness is an important parameter that has impact on wear resistance, as well as the resistance to erosion-corrosion. Vickers micro-hardness (HV) is the standard approach used to assess the hardness of thermal spray coatings. In the specific case of thermal spray coatings, a 300-gram load is frequently used, since it is believed that this load and the affected area are large enough to produce a measurement that is averaged over any macro-porosity that may be present. These authors also like to report micro-hardness measurements with a 100-gram load, since it is believed that this load and the affected area are smaller, and therefore capable of sampling bulk material properties. Typical ranges of the measured micro-hardness for these HVOF coatings are summarized in Table 4.

Cyclic Polarization – Passive Film Stability

Spontaneous breakdown of the passive film and localized corrosion require that the open-circuit corrosion potential exceed the critical potential:

$$E_{corr} \geq E_{critical}$$

The resistance to localized corrosion is quantified through measurement of the open-circuit corrosion potential (E_{corr}), the breakdown potential ($E_{critical}$) and the repassivation potential (E_{rp}). The greater the difference between the open-circuit corrosion potential and the repassivation potential (ΔE), the more resistant a material is to modes of localized corrosion such a pitting and crevice corrosion. In integrated corrosion models, general corrosion is invoked when E_{corr} is less than $E_{critical}$ ($E_{corr} < E_{critical}$), and localized corrosion is invoked when E_{corr} exceeds $E_{critical}$ [13]. The data provided in this publication are sufficient to establish when general and localized

corrosion occur, and the rates of general corrosion are when general corrosion is invoked. Note that these data only apply for the environments explored during testing.

Cyclic polarization (CP) is used as a means of measuring the critical potential ($E_{critical}$) of corrosion resistant materials, relative to their open-circuit corrosion potential (E_{corr}). In the published scientific literature, different bases exist for determining the critical potential from electrochemical measurements. The critical potential is frequently defined as the point where the passive current density increases during the forward (anodic) scan to a level between 1 to 10 $\mu A/cm^2$ (10^{-6} to 10^{-5} A/cm^2). Alternative definitions of the repassivation potential are used. One definition is the point during the reverse (cathodic) scan where the current density drops to a level indicative of passivity, which is *assumed* to be between 0.1 to 1 $\mu A/cm^2$ (10^{-6} to 10^{-7} A/cm^2). An alternative definition is the point where the forward and reverse scans intersect, a point where the current density being measured during the reverse scan drops to a level *known* to be indicative of passivity. These authors prefer the latter definition.

Definitions of the threshold and repassivation potentials vary from investigator to investigator. Gruss et al. define the repassivation potential as the point where the current density drops to 10^{-6} to 10^{-7} A cm^{-2} [23]. Scully et al. define the threshold potential for crevice corrosion of Alloy 22 as the point during the scan of electrochemical potential in the forward direction where the current density increases to a level of 10^{-6} to 10^{-5} A cm^{-2}. Scully et al. generated CP data with very tight crevices and concentrated electrolytes consisting of 5M LiCl, 0.024 to 0.24M $NaNO_3$, 0.026 to 0.26M Na_2SO_4 and HCl [27]. Testing was conducted at two temperature levels, 80 and 95°C. The crevices were formed with a multiple crevice former, PTFE tape, and an applied torque of 70 inch pounds. Under these circumstances, some electrochemical activity indicative of crevice corrosion was observed at potentials ranging from 71 to 397 mV versus Ag/AgCl, depending upon the composition of the electrolyte. Using a current density criterion for repassivation of 10^{-5} A cm^{-2}, repassivation potentials were determined to be slightly above, but relatively close to the open-circuit corrosion potential.

Cyclic polarization measurements have been based on a procedure similar to ASTM (American Society for Testing and Materials) G 5 standard with slight modification [28-31]. The ASTM G 5 standard calls for a 1N H_2SO_4 electrolyte, whereas synthetic bicarbonate, sulfate-chloride, chloride-nitrate, and chloride-nitrate solutions, with sodium, potassium and calcium cations, as well as natural seawater have been used for this investigation. The chloride anion promotes passive film breakdown, while the nitrate serves as an inhibitor. Furthermore, the ASTM G 5 standard calls for the use of de-aerated solutions, whereas aerated and de-aerated solutions were used here. After a 24-hour hold period, during which the open circuit corrosion potential is determined, the potential is scanned in the positive (anodic) direction from a level slightly more negative than the corrosion potential (cathodic limit), to a reversal potential (E_{rev}) near that required for oxygen evolution (anodic level). During the positive scan, anodic oxidation peaks may be observed (centered at E_{peak}) that have been correlated with the oxidation of molybdenum at the alloy surface (passive film), as well as current excursions that are usually associated with breakdown of the passive film. During the negative (cathodic) scan, a hysteresis loop will be observed in cases where passivity has been lost. As the scan continues, the current density may eventually decrease to a level equivalent to that experienced during the positive scan, and

indicative of reformation of the passive film. The potential at which this occurs is known as the repassivation potential (E_{rp}).

Temperature-controlled borosilicate glass (Pyrex) electrochemical cells were used for cyclic polarization and other similar electrochemical measurements. This cell has three electrodes, a working electrode (test specimen), the reference electrode, and the counter electrode. A standard silver silver-chloride electrode, filled with near-saturation potassium chloride solution, is used as the reference, and communicates with the test solution via a Luggin probe placed in close proximity to the working electrode, thereby minimizing Ohmic losses. Numerical corrections for the reference electrode junction potential have been estimated, and have been found to be insignificant. The electrochemical cell is equipped with a water-cooled junction to maintain reference electrode at ambient temperature, thereby maintaining integrity of the potential measurement, and a water-cooled condenser to prevent the loss of volatile species from the electrolyte. All powder used to produce these coatings was produced by The NanoSteel Company (TNC), and the HVOF coatings used to generate the data in this publication were produced by Plasma Technology Incorporated (PTI). Synthetic brine solutions (5M $CaCl_2$ and others) were prepared at Lawrence Livermore National Laboratory with reagent-grade chemicals and de-ionized water. The natural seawater used in these tests was obtained directly from Half Moon Bay along the northern coast of California, and was transported to the laboratory in a clean polyethylene container. This Half Moon Bay seawater is referred to as natural seawater in this publication.

Cyclic Polarization – Alloy Screening

Cyclic polarization of melt spun ribbons was further used to compare the relative corrosion resistance of a large number candidate alloy compositions in near-boiling natural seawater at 90°C. As previously discussed, the alloy compositions explored during this study are summarized in Tables 1 and 2. The difference between the open circuit corrosion potential (E_{corr}) and the repassivation potential (E_{rp}) was used as a basis of comprison for the relative corrosion performance of candidate alloys. Several of the candidate alloy compositions had a larger metric value (E_{rp}- E_{corr}) than the reference material, which has been established as nickel-based Alloy C-22, due to its own outstanding corrosion performance. During this early phase of the study, it was concluded that several types of iron-based amorphous metals exist which all have passive film stabilities in seawater at 30°C and 90°C that are comparable to that of the reference material.

Potentiostatic Step – Threshold for Passive Film Breakdown

Potentiostatic step tests have been used to determine the potential at which the passive film breaks down on the reference material, Alloy C-22, and on the two amorphous metals of primary interest, SAM2X5 and SAM1651. During prolonged periods of at a constant applied potential (potentiostatic polarization), which are typically 24 hours in duration, the current is monitored as a function of time. In cases where passivity is lost, the current increases, and the test sample is aggressively attacked. In cases where passivity is maintained, the current decays to a relatively constant asymptotic level, consistent with the known passive current density. In these tests, periods of polarization are preceded by one hour at the open circuit corrosion potential.

All were tested in natural seawater heated to 90°C. To eliminate the need for surface roughness corrections in the conversion of measured current and electrode area to current density, the SAM2X5 coatings were polished to a 600-grit finish prior to testing. The constant potential denoted in figures was applied after 1 hour at the open circuit corrosion potential (OCP).

Effect of Devitrification on Corrosion Resistance

To assess the sensitivity of these iron-based amorphous metals to devitrification, which can occur at elevated temperature, melt-spun ribbons of Fe-based amorphous metals were intentionally devitrified by heat treating them at various temperatures for one hour. After heat treatment, the samples were evaluated in low temperature seawater (30°C), to determine the impact of the heat treatment on passive film stability and corrosion resistance. The temperatures used for the heat treatment were: 150, 300, 800 and 1000°C. Untreated (as received) ribbons were also tested, and provide insight into the baseline performance.

Determining Corrosion Rate with Linear Polarization

The linear polarization method has been used as a method for determining the corrosion rates of the various amorphous metal coatings, including SAM2X5 and SAM1651. This method is based upon experimental determination of electrokinetic parameters in the classic Tafel equation with a potentiostat. The classic Butler-Volmer expression collapses into the well-known anodic Tafel equation at high anodic potential, where the contribution of the electrochemical reduction (cathodic) reaction to the overall current at the electrode surface becomes insignificant (defined as < 1%). At high cathodic potential, where the contribution of the electrochemical oxidation (anodic metal dissolution) reaction to the net electrode current is insignificant, the Butler-Volmer expression becomes the cathodic Tafel equation. The procedure used for linear polarization testing consists of the following steps: (1) hold the sample for ten (10) seconds at the open circuit potential (OCP); (2) beginning at a potential 20 mV below the OCP (OCP-20 mV), increase the potential linearly at a constant rate of 0.1667 mV per second, to a potential 20 mV above the OCP (OCP+20 mV); (3) record the current being passed from the counter electrode to the working electrode by the potentiostat, as a function of potential relative to the standard/silver silver-chloride (Ag/AgCl) reference electrode; and (4) determine the parameters in the cathodic Tafel line by performing linear regression on the voltage-current data from 10 mV below the OCP (OCP − 10 mV) to 10 mV above the OCP (OCP + 10 mV). The slope of this line is the polarization resistance, *Rp* (ohms), which is defined as [33]:

$$R_P = \left(\frac{\partial E}{\partial I} \right)_{E_{corr}}$$

A parameter (B) is defined in terms of the slopes of the anodic and cathodic branches of the Tafel line:

$$B = \frac{\beta_a \beta_c}{2.303(\beta_a + \beta_c)}$$

Values of B are published for a variety of iron-based alloys, and vary slightly from one alloy-environment combination to another [33]. Values for carbon steel, as well as Type 304, 304L and 430 stainless steels, in a variety of electrolytes which include seawater, sodium chloride, and sulfuric acid, range from 19 to 25 mV. A value for nickel-based Alloy 600 in lithiated water at 288°C is given as approximately 24 mV. While no values have yet been developed for the Fe-based amorphous metals that are the subject of this investigation, it is believed that a conservative representative value of approximately 25 mV is appropriate for the conversion of polarization resistance to corrosion current. Given the value for Alloy 600, a value of 25 mV is also believed to be acceptable for converting the polarization resistance for nickel-based Alloy C-22 to corrosion current. The corrosion current, I_{corr} (A) is then defined as:

$$I_{corr} = \frac{B}{R_p}$$

where the parameter B is conservatively assumed to be approximately 25 mV. The corrosion current density, i_{corr} (A cm^{-2}), is defined as the corrosion current, normalized by electrode area, and is:

$$i_{corr} = \frac{I_{corr}}{A}$$

A is the surface area of the sample in square centimeters (cm^2). The corrosion (or penetration) rate of an alloy can be calculated from the corrosion current density with the following formula derived from Jones [34]:

$$\frac{dp}{dt} = \frac{i_{corr}}{\rho_{alloy} n_{alloy} F}$$

where p is the penetration depth, t is time, i_{corr} is the corrosion current density, ρ_{alloy} is the density of the alloy (g cm^{-3}) , n_{alloy} is the number of gram equivalents per gram of alloy, and F is Faraday's constant. The value of n_{alloy} can be calculated with the following formula:

$$n_{alloy} = \sum_j \left(\frac{f_j n_j}{a_j} \right)$$

where f_j is the mass fraction of the jth alloying element in the material, n_j is the number of electrons involved in the anodic dissolution process, which is assumed to be congruent, and a_j is the atomic weight of the jth alloying element. Congruent dissolution means that the dissolution rate of a given alloy element is proportional to its concentration in the bulk alloy. These equations have been used to calculate factors for the conversion of corrosion current density to the penetration rate (corrosion rate). Equivalent alternative expressions have also been published [MRSxxx]. These conversion factors are summarized in Tables 5.

Effects of Junction Potential on Electrochemical Measurements

It is important to understand the magnitude of the error in the potential measurements due to the junction potential. A correction has been performed based upon the Henderson Equation, as presented by Bard and Faulkner [35]. The calculated junction for several test solutions have been estimated with ionic properties used in the calculation were also taken from Bard and Faulkner. These corrections are not very large, with the largest being less than approximately 10 mV. This value corresponds to the junction potential for SSW at 90°C. It is concluded that insignificant error results from neglecting to correct for the junction potential.

Validation with Salt Fog Testing

The corrosion resistance of the amorphous metal coatings was verified during salt fog testing. As previously discussed, the salt fog test was used to compare various wrought ant thermal-spray alloys, melt-spun ribbons, arc-melted drop-cast ingots, and thermal-spray coatings for their susceptibility to corrosion by salt sprays, like those that might be encountered aboard naval ships. This test is also known as the salt spray test. The most recent tests have focused on reference materials, including the SAM40 master alloy, and the SAM2X5 and SAM1651 amorphous metal formulations, in the form of arc-melted drop-cast ingots, melt-spun ribbons, and high-velocity oxy-fuel coatings with no significant porosity and near theoretical density. In contrast, the first tests focused on early thermal-spray coatings, which had residual porosity and crystalline structure, and lower resistance to corrosion.

Both salt fog tests were conducted according to the standard General Motors (GM) salt fog test, identified as GM9540P, which is similar to the standard American Society for Testing and Materials (ASTM) salt fog test, which is identified as ASTM B117 and entitled “Standard Test Method of Salt Spray (Fog) Testing.” The test protocol for GM9540P is summarized in Table 6. Samples of iron-based amorphous-metal thermal spray coatings and several reference samples were evaluated with the GM9540P test protocol. The four reference samples included Type 316L stainless steel, nickel-based Alloy C-22 (N06022), Ti Grade 7, and the 50:50 nickel-chromium binary.

Composition of Amorphous Metals

The composition of the SAM2X-series of melt-spun ribbons has been verified with energy dispersive spectroscopy, as shown in Figures 1 and 2, and summarized in Table 2. The EDS data shown in Figures 1 provides the relative abundance of molybdenum in SAM2X1, SAM2X3, SAM2X5 and SAM2X7 melt-spun ribbons, which were prepared by adding three, five and seven atomic percent (1, 3, 5 and 7 atomic %) molybdenum to SAM40, respectively. The SAM2X5 composition appears to provide adequate corrosion resistance, and is a formulation that can still be processed with relative ease. The SAM2X7 composition has a higher calculated pitting-resistance equivalence number (PREN) than the alloys with less molybdenum, and slightly better corrosion resistance than SAM2X5, but is somewhat more difficult to make. Figure 2 is a comparison of the spectra shown in Figure 1, but with an expanded energy scale, with a maximum energy being approximately 4 keV. The molybdenum peak is presented with greater clarity by using the expanded scale.

EXPERIMENTAL RESULTS

Melt-Spun Ribbons

Melt-spun ribbons prepared by The NanoSteel Company (TNC) were characterized with XRD. Figure 3a shows the resulting diffraction patterns of melt-spun ribbons of two austenitic alloys, nickel-based Alloy C-22 and Type 316L stainless steel, which clearly indicate that both of these materials are indeed crystalline, and that the melt spinning process cannot capture the amorphous meta-stable state for these compositions

Figure 3b shows X-ray diffraction data for melt-spun ribbon (MSR) samples of iron-based amorphous metals identified as: (a) SAM40; (b) SAM2X1; (c) SAM2X3; (d) SAM2X5; and (e) SAM2X7. These data are clearly indicative of amorphous structure, and a complete lack of crystalline structure, which is attributed to the relatively high concentrations of boron.

Gas Atomized Powders

The absence of crystalline structures is generally believed to be one factor that contributes to the corrosion resistance of amorphous alloys [14-16]. It was hypothesized that a relationship may exist between powder size, residual crystallinity, mechanical properties and corrosion resistance. A portion of this investigation was directed towards the proof or disproof of this hypothesis. The crystalline structure of powders can vary with particle size, since different cooling rates are experienced by particles with different sizes. Particle size sensitivity is explored in this publication, in regard to the residual crystalline phases present in powders and coatings, as well as in regard to the impact of those crystalline phases on the corrosion resistance of coatings. A correlation has been observed between the formation of substantial amounts of deleterious crystalline phases, such as ferrite, in Fe-based amorphous metals, and the susceptibility to corrosion in chloride-containing environments [1].

Due to the relatively high critical cooling rate of SAM2X5 in comparison to that of SAM1651, technological challenges had to be overcome to produce completely amorphous powder with this high-boron Fe-based amorphous metal. It has been found that particular care must be paid to the control of raw material feedstock, conditions within the atomization process. Through careful control of these variables, completely amorphous powders have been produced with the SAM2X5 high-boron composition. It should be noted that the particle size distribution of powders typically used as feedstock for HVOF deposition processes lies between 15 and 53 microns (–53/+15 μm). To explore the impact of particle size on the residual crystalline content of coatings, as well as the corrosion resistance of these coatings, a larger number of particle size distributions have been explored. Thus, this work provide unique insight into the relationship between particle size, as it effects the critical cooling rate along the radius of the particles, residual crystalline structure in the produced coatings, and the corresponding corrosion resistance.

The corrosion performance of thermal spray coatings of iron-based amorphous metals depends upon the quality of the powder used to produce the coating. In general, completely amorphous powders are required for the deposition of completely amorphous coating with the desired level of corrosion resistance. Note that the powders are usually softened during thermal spray, and not remelted, so the original degree of crystalline or amorphous structure is preserved. Substantial

experience has now been gained with a wide range of powders, having various levels of residual crystalline phase present. A scanning electron micrograph (SEM) image of SAM2X5 iron-based amorphous-metal powder is presented in Figure 4, and shows spherical morphology, which is essential for good flow characteristics in thermal spray processes.

Thermal Spray Coatings

XRD data for a HVOF coating of SAM2X5 on nickel-based Alloy C-22 substrate, and deposited with with a JP5000™ thermal-spray gun (Praxair TAFA JP5000 System), is shown in Figure 5. This coating also had residual crystalline phases present, and was prepared with Lot # 04-265 powder, which had a broad range of particle sizes (–53/+15μm). Residual crystalline phase have been tentatively identified as bcc ferrite and Cr_2B.

XRD data for a HVOF coating of SAM2X5 on Type 316L stainless steel substrate, deposited with the JK2000™ thermal spray gun (Deloro Stellite JetKote JK2000 System), is shown in Figure 6. This coating was prepared with Lot # 04-200 powder which had a broad range of particle sizes (–53/+15μm), typically used for HVOF processes. XRD data for a HVOF coating of SAM2X5 on Type 316L stainless steel substrate, deposited with JK2000 thermal spray gun is shown in Figure 7. This coating was prepared with Lot # 04-199 powder which had a broad range of particle sizes (–30/+15μm).

Thermal Properties

The thermal properties of these Fe-based amorphous metals have been determined by Perepezko and Hildal. SAM2X5 has a glass transition temperature of ~579°C, a crystallization temperature of ~628°C, a melting point of ~1133°C, and a reduced glass transition temperature of ~0.57 (with a value of 0.6 being ideal). SAM2X7, an alloy in the same family as SAM2X5, has a glass transition temperature of ~573°C, a crystallization temperature of ~630°C, a melting point of ~1137°C, and a reduced glass transition temperature of 0.57. In contrast, the yttrium-containing SAM1651 formulation has a glass transition temperature of ~584°C, a crystallization temperature of ~653°C, a melting point of ~1121°C, and a reduced glass transition temperature of ~0.55. The critical cooling rates for SAM2X7 and SAM1651, have been determined to be ~ 610 and ≤ 80 K per second, respectively. Clearly, the yttrium additions in SAM1651 enhance glass-forming ability of these materials. The data for the SAM2X-series of alloys is summarized in Table 3.

Cyclic Polarization Data – Screening Tests

Potential-current data obtained during the cyclic polarization (CP) of a SAM40 melt-spun ribbon (MSR) in natural seawater at 30°C is shown in Figure 8. The OCP was –0.296 V verses Ag/AgCl, and the current density measured between OCP and 0.9 volts was below 1 $\mu A/cm^2$, which is indicative of passivity, with a distinct anodic oxidation peak was observed at approximately 0.5 V, which is believed to be due to the oxidation of molybdenum in the passive film.

Potential-current data for two wrought Alloy C-22 samples and a SAM2X7 MSR in natural seawater at 30°C is shown in Figure 9. In general, the measured current densities for the SAM2X series of iron-based amorphous-metal melt-spun ribbons were less than those measured for

wrought samples of Alloy C-22, indicating better passivity of the amorphous metals. The anodic oxidation peaks for SAM2X7 (see previous figure) and Alloy C-22 are believed to be due to the oxidation of molybdenum.

Potential-current data for two wrought Alloy C-22 samples, and an as-sprayed HVOF coating of SAM2X5, which was deposited on a Type 316L stainless steel substrate, in natural seawater at 90°C is shown in Figure 10. In general, the measured current density for the iron-based amorphous-metal thermal-spray coating in heated seawater was less than those measured for wrought samples of Alloy C-22, indicating better passivity of HVOF SAM2X5 coating in this particular environment. The distinct anodic oxidation peaks for Alloy C-22, and the faint peak for the SAM2X5 thermal spray coating, are all believed to be due to the oxidation of molybdenum.

Potentiostatic Data – Passive Film Stability

Potential-step testing has been performed on wrought Alloy C-22 (reference material); fully dense and completely amorphous melt spun ribbons of SAM2X5; optimized HVOF coatings produced with −53/+30 micron powders of SAM2X5; and optimized HVOF coatings produced with −30/+15 micron powders of SAM2X5, as shown in Figure 11. These coatings were produced with SAM2X5 powder supplied by The NanoSteel Company (TNC), and deposited by the University of California in Davis, California (UCD) and Plasma Tech Incorporated (PTI) in Torrance, California. All were tested in natural seawater heated to 90°C. To eliminate the need for surface roughness corrections in the conversion of measured current and electrode area to current density, the SAM2X5 and SAM1651 coatings were polished to a 600-grit finish prior to testing. The curves represent the asymptotic current density reached after 24 hours at the corresponding potential (each data point represents a 24 hour test). The constant potential was applied after 1 hour at the open circuit corrosion potential (OCP). From previous work presented in the FY04 Annual Report (given in references), it has been found that coatings produced with SAM2X5 powders below a critical size are fully dense and are completely amorphous. The coatings produced with finer powders are therefore expected to have lower porosity and less residual crystalline phases present than those produced with larger particles. These data enable a clear and unambiguous determination of the threshold potentials for passive film breakdown in a non-creviced condition. First, it is clear that the passive film on wrought Alloy C-22 commences breakdown at a potential of approximately 200 mV relative to a standard Ag/AgCl reference electrode (approximately 600 mV above the open circuit corrosion potential), and has the least corrosion resistance of any sample evaluated during this test. Passive film breakdown on the SAM2X5 melt-spun ribbon did not occur until a potential in excess of 1200 mV verses Ag/AgCl (1400 mV above OCP) was applied. Furthermore, the observed passive current density observed with this sample was extremely low. Both HVOF coatings of SAM2X5 (large and small powder sizes) also exhibited outstanding passive film stability, superior to that of the reference material. The passive film on the coating produced with −30/+15 micron powder remained intact until application of 1000 mV verses Ag/AgCl (1200 mV above OCP), with a current density well within the passive range of several microamps per square centimeter. Similar observations were made with the coating produced with −53/+30 micron powders. Any differences in morphology did not have significant impact on corrosion resistance.

MRS]s Figures 12 through 17 show measured transients in current density at a constant applied potentials of 900, 1000, 1100, 1200, 1300 and 1400 mV verses OCP for several different materials in natural seawater at 90°C. The materials compared in each figure include wrought Alloy C-22 (reference material), a fully dense and completely amorphous melt-spun ribbon (MSR) of SAM2X5, HVOF coatings produced with –53/+30 micron powders of SAM2X5, and HVOF coatings produced with –30/+15 micron powders of SAM2X5. The constant potential was applied after 1 hour at the open circuit corrosion potential (OCP). The passive film on the melt spun ribbon and HVOF coatings of SAM2X5 is more stable than that on wrought nickel-based Alloy C-22 under these conditions, leading to the conclusion that this iron-based amorphous metal has superior corrosion resistance.

Transients in current density at a constant applied potential of 900 mV verses OCP for wrought Alloy C-22 (reference material), a fully dense and completely amorphous MSR of SAM2X5, HVOF coatings produced with –53/+30 micron powders of SAM2X5, and HVOF coatings produced with –30/+15 micron powders of SAM2X5, all in natural seawater heated to 90°C, are compared in Figure 12. The constant potential was applied after 1 hour at the open circuit corrosion potential (OCP). It should also be noted that the periodic current fluctuations observed during testing of Alloy C-22 are real, and are indicative of the onset of localized corrosion. The HVOF coating prepared with relatively fine (–30/+15 μm) SAM2X5 powder has a temporary loss of passivity at 5×10^4 seconds, but undergoes repassivation at 5×10^4 seconds. In contrast, the coating produced with the standard HVOF cut of powder (–53/+30 μm) appears to be completely stable, as does the melt-spun ribbon. The differences in the corrosion resistance of the SAM2X5 coatings produced with relatively coarse (–53/+30 μm) and relatively fine (–30/+15 μm) powders is not well understood, but may be related to differences in surface area. The passive film on the melt spun ribbon and HVOF coatings of SAM2X5 is more stable than that on wrought nickel-based Alloy C-22 under these conditions, leading to the conclusion that this iron-based amorphous metal has superior corrosion resistance.

Transients in current density at a constant applied potential of 1000 mV verses OCP for wrought Alloy C-22 (reference material), a fully dense and completely amorphous MSR of SAM2X5, HVOF coatings produced with –53/+30 micron powders of SAM2X5, and HVOF coatings produced with –30/+15 micron powders of SAM2X5, all in natural seawater heated to 90°C, are compared in Figure 13. The constant potential was applied after 1 hour at the open circuit corrosion potential (OCP). The passive film on the melt spun ribbon and HVOF coatings of SAM2X5 is more stable than that on wrought nickel-based Alloy C-22 under these conditions, leading to the conclusion that this iron-based amorphous metal has superior corrosion resistance.

Transients in current density at a constant applied potential of 1100 mV verses OCP for wrought Alloy C-22 (reference material), a fully dense and completely amorphous MSR of SAM2X5, HVOF coatings produced with –53/+30 micron powders of SAM2X5, and HVOF coatings produced with –30/+15 micron powders of SAM2X5, all in natural seawater heated to 90°C, are compared in Figure 14. The constant potential was applied after 1 hour at the open circuit corrosion potential (OCP). In this case, the passivity of Alloy C-22 was completely lost, with a dramatic increase in the observed current density to levels between 80 and 90 $\mu A/cm^2$, with dramatic attack of the Alloy C-22. A significant difference was observed between the corrosion

resistance of HVOF SAM2X5 coatings produced with coarse (–53/+30 μm) and fine (–30/+15 μm) powders, with the standard coarse powder having better performance. The coating produced with the finer powder (–30/+15 μm) did not exhibit good passivity, defined as a current density less than approximately 5 $\mu A/cm^2$, until 2×10^4 seconds, with fluctuations in current density that may be indicative of localized corrosion phenomena. Passivity appears to have been compromised at 7×10^4 seconds. The coating produced with the coarse (–53/+30 μm) powder and the melt-spun ribbon both maintained exceptional passivity during the entire test. In summary, the passive film on the melt spun ribbon and HVOF coatings of SAM2X5 is more stable than that on wrought nickel-based Alloy C-22 under these conditions, leading to the conclusion that this iron-based amorphous metal has superior corrosion resistance.

Transients in current density at a constant applied potential of 1200 mV verses OCP for wrought Alloy C-22 (reference material), a fully dense and completely amorphous MSR of SAM2X5, HVOF coatings produced with –53/+30 micron powders of SAM2X5, and HVOF coatings produced with –30/+15 micron powders of SAM2X5, all in natural seawater heated to 90°C, are compared in Figure 15. The constant potential was applied after 1 hour at the open circuit corrosion potential (OCP). The Alloy C-22 samples lost all passivity, while the SAM2X5 HVOF coatings and melt-spun ribbons maintained passivity, with current pulses that may be indicative of incipient localized corrosion phenomena observed during the testing of the coatings produced with the finer (–30/+15 μm) powder. The passive film on the melt spun ribbon and HVOF coatings of SAM2X5 is more stable than that on wrought nickel-based Alloy C-22 under these conditions, leading to the conclusion that this iron-based amorphous metal has superior corrosion resistance.

Transients in current density at a constant applied potential of 1300 mV verses OCP for wrought Alloy C-22 (reference material), a fully dense and completely amorphous MSR of SAM2X5, HVOF coatings produced with –53/+30 micron powders of SAM2X5, and HVOF coatings produced with –30/+15 micron powders of SAM2X5, all in natural seawater heated to 90°C, are compared in Figure 16. The constant potential was applied after 1 hour at the open circuit corrosion potential (OCP). Observations here are similar to those discussed in regard to Figure 16, with the passive current densities observed with the SAM2X5 HVOF coatings prepared with the coarser powders beginning to exceed those observed with the coatings prepared with the finer powders. The passive film on the melt spun ribbon and HVOF coatings of SAM2X5 is more stable than that on wrought nickel-based Alloy C-22 under these conditions, leading to the conclusion that this iron-based amorphous metal has superior corrosion resistance.

Transients in current density at a constant applied potential of 1400 mV verses OCP for wrought Alloy C-22 (reference material), a fully dense and completely amorphous MSR of SAM2X5, HVOF coatings produced with –53/+30 micron powders of SAM2X5, and HVOF coatings produced with –30/+15 micron powders of SAM2X5, all in natural seawater heated to 90°C, are compared in Figure 17. The constant potential was applied after 1 hour at the open circuit corrosion potential (OCP). Clearly the passivity on the Alloy C-22 is lost under these aggressive conditions, with the current density pulsing to 10 mA/cm^2 and decaying to 2 mA/cm^2. In contrast, the SAM2X5 samples remained passive with current densities of only 1-5 $\mu A/cm^2$. However, at this high applied potential, the passive current density observed with the coating produced with the coarse (–53/+30 μm) powder, or that observed with the melt-spun ribbon. The

passive film on the melt spun ribbon and HVOF coatings of SAM2X5 is more stable than that on wrought nickel-based Alloy C-22 under these conditions, leading to the conclusion that this iron-based amorphous metal has superior corrosion resistance.

Transients in current density at various levels of constant applied potential ranging from 100 to 1400 mV verses OCP for Alloy C-22 in natural seawater at 90°C are shown in Figure 18. This reference material was polished to a 600-grit finish. The constant potential was applied after 1 hour at the open circuit corrosion potential (OCP). Passive film stability is lost above 700 mV verses OCP.

Transients in current density at various levels of constant applied potential ranging from 100 to 1600 mV verses OCP for a melt-spun ribbon of SAM2X5 in natural seawater at 90°C are indicative of good passive film stability, and are shown in Figure 19. The constant potential was applied after 1 hour at the open circuit corrosion potential (OCP). The passive film stability of this SAM2X5 sample is maintained at potentials up to 1500 mV verses OCP, which is approximately 800 mV higher than the critical potential observed with Alloy-C22. At an applied potential of 1600 mV verses OCP, passivity is lost after several hours.

Transients in current density at various levels of constant applied potential ranging from 100 to 1500 mV verses OCP for a recently optimized SAM2X5 HVOF coating (–30/+15 micron powder) in deaerated natural seawater at 90°C are indicative of good passive film stability, and are shown in Figure 20. The constant potential was applied after 1 hour at the open circuit corrosion potential (OCP). To eliminate the need for surface roughness corrections in the conversion of measured current and electrode area to current density, the SAM2X5 coating was polished to a 600-grit finish prior to testing. The curves represent the asymptotic current density reached after 24 hours at the corresponding potential (each data point represents a 24 hour test). The specified fixed potential was applied after 1 hour at the open circuit corrosion potential (OCP). The passive film stability of this SAM2X5 sample is maintained at potentials up to 1400 mV verses OCP, which is approximately 700 mV higher than the critical potential observed with Alloy-C22. At an applied potential of 1500 mV verses OCP, passivity is lost after several hours.

Transients in current density at various levels of constant applied potential ranging from 100 to 1500 mV verses OCP for a recently optimized SAM2X5 HVOF coating (–53/+30 micron powder) in natural seawater at 90°C are indicative of exceptional passive film stability, and are shown in Figure 21. To eliminate the need for surface roughness corrections in the conversion of measured current and electrode area to current density, the SAM2X5 coatings were polished to a 600-grit finish prior to testing. The constant potential was applied after 1 hour at the open circuit corrosion potential (OCP). The passive film stability of this SAM2X5 sample is maintained at potentials up to 1400 mV verses OCP, which is approximately 700 mV higher than the critical potential observed with Alloy C-22. At an applied potential of 1500 mV verses OCP, passivity is lost after several hours.

Effects of Thermally-Driven Devitrification – Alloy Stability

To assess the sensitivity of these iron-based amorphous metals to devitrification, which can occur at elevated temperature, melt-spun ribbons of SAM40 were intentionally devitrified by heat treating them at various temperatures for one hour. Heat treatment for one hour above the

crystallization temperature causes the onset of crystalline phase formation, which has been shown to be deleterious to corrosion resistance. Figure 22 shows X-ray diffraction (XRD) data for SAM40, SAM2X5 and SAM1651 amorphous metal ribbons annealed at various temperature levels up to 800°C. As expected, crystalline peaks appear at temperatures above the crystallization temperature.

The effects devitrification on the electrochemical corrosion behavior of these materials has been investigated, with the results for SAM2X5 reported here. After heat treatment, the samples were evaluated in low temperature seawater (30°C), to determine the impact of the heat treatment on passive film stability and corrosion resistance. The temperatures used for the heat treatment were: 150, 300, 800 and 1000°C. Untreated (as received) ribbons were also tested, and provide insight into the baseline performance. These samples showed no significant hysteresis and change in repassivation potential at heat treatments of 150-300°C, but showed a dramatic loss of corrosion resistance when heat treatments were performed at 800-1000°C, which are above the known crystallization temperature of approximately 600-650°C (623°C) given in Table 3. Both ribbons treated at elevated temperature show large hysterisis loops, which are indicative of passive film breakdown, with a clearly defined repassivation potential near -600 mV verses Ag/AgCl (about 100 mV above the OCP). The operational limit for these materials, when being used for corrosion resistance, appears to be bounded by the crystallization temperature.

Melt spun ribbons of SAM2X5 were also intentionally devitrified by heat treating at 800°C for one hour and then subjected to cyclic polarization in 5M $CaCl_2$ at 105°C. In comparison to the as-received sample, the sample heat-treated at 800°C showed a dramatic loss of corrosion resistance, as shown in Figure 23. As discussed in regard to the preceding figure, this heat-treatment temperature was known to be above the crystallization temperature of approximately 600-650°C (623°C) given in Table 3. The heat-treated ribbon showed a large hysterisis loop in the hot concentrated calcium chloride solution, which is indicative of passive film breakdown, with a clearly defined repassivation potential neat the OCP. The post heat-treatment microstructural characterization with electron microscopy and X-ray diffraction by Yang et al. verify the existence of a completely amorphous material below the crystallization temperature, and the development of crystalline precipitates during heat treatment above this limit. These electron microscopy images may also indicate that the corrosive attack of the precipitated crystalline phases occur to a depth of approximately 10 microns. When being used for corrosion resistance in hot geothermal brines such as calcium chloride, the operational limit also appears to be bounded by the crystallization temperature.

Linear Polarization Data – Corrosion Rates

Linear polarization was used to determine the approximate corrosion rates of the thermal spray coatings of amorphous metals of interest (HVOF SAM2X5 and other coatings) and the reference material (wrought nickel-based Alloy C-22) in three relevant environments, natural seawater at two temperature levels, and in hot concentrated calcium chloride (5M $CaCl_2$ at 105°C). Values of the corrosion potential, polarization resistance, corrosion current density, and corrosion rate are summarized in Table 7 and Figures 24 through 26. In seawater at both 30 and 90°C, the corrosion rates of HVOF SAM2X5 coatings exhibited slightly lower corrosion rates than either wrought sample of Alloy C-22. The corrosion rates of all materials increased with temperature,

as expected. In calcium chloride at 105°C, the corrosion rates of HVOF SAM2X5 coatings were comparable to, or slightly lower than that of wrought Alloy C-22. In general, the corrosion rates observed in the hot calcium chloride (105°C) were higher than those observed in the heated seawater (90°C), which was also expected.

Salt Fog Testing – Verification of Corrosion Resistance

As shown in Figure 27, salt fog testing was conducted by Aprigliano on several thermal spray coatings, including HVOF coatings of Alloy C-22, Type 316L stainless steel, SAM40 (also referred to as DAR40), SAM2X5 (also referred to as LDAR2X5) and other amorphous-metal formulations of interest. After 13 cycles in the GM9540P salt fog test, the HVOF coatings of Type 316L stainless steel and SAM40 showed substantial corrosion. Very slight rust spots were observed on the C-22 coating. In contrast, the newer SAM2X5 formulations showed no corrosion at 30 cycles. The testing was continued to almost 60 cycles, with no evidence of corrosion observed with SAM2X5 and other amorphous-metal formulations of interest.

DISCUSSION

Issues to be resolved in the future include the performance of these coatings in other environments, which cover a broader range of salt concentrations, both lower and higher pH, and even higher temperatures. More information is required on the mechanical properties of these coatings, including measurements of the fracture stress and strain, the susceptibility to stress corrosion and hydrogen induced cracking, and the strength of the interfacial bond between the substrate and coating. The absorption of hydrogen by these materials should also be investigated.

The reference material, nickel-based Alloy C-22, is an outstanding corrosion-resistant engineering material. Even so, crevice corrosion has been observed with C-22 in hot sodium chloride environments without buffer or inhibitor. Comparable metallic alloys such as SAM2X5 and SAM1651 may also experience crevice corrosion under sufficiently harsh conditions. Accelerated crevice corrosion tests are now being conducted to intentionally induce crevice corrosion, and to determine those environmental conditions where such localized attack occurs.

CONCLUSIONS

The hypothesis that the corrosion resistance of Fe-based amorphous metals can be enhanced through application of heuristic principles related to the additions of chromium, molybdenum and tungsten has been tested, and found to have merit. The decision to achieve enhanced corrosion resistance in these Fe-based amorphous metals was initially based upon two considerations. First, substantial enhancements in corrosion resistance had been observed in stainless steels and nickel based alloys by adding molybdenum, as well as other alloying elements. Secondly, this enhancement in localized corrosion resistance can be quantified in the pitting resistance equivalence number, and could be used as a guide to determine the level of molybdenum addition necessary to achieve localized corrosion resistance comparable to nickel-based Alloy C-22, one of the benchmark materials. Electrochemical tests have been used to prove that corrosion performance comparable to wrought and thermally sprayed coatings of nickel-based Alloy C-22 can be achieved with the new Fe-based amorphous metals in hot

concentrated calcium chloride and seawater. The passive film on Alloy C-22 in seawater at 90°C begins to breakdown at an applied potential of 200 mV verses OCP, and breaks down catastrophically at 1000 mV verses OCP, whereas SAM2X5 maintains passivity at applied potentials as high as 1400 mV verses OCP in the same environment.

Early HVOF coatings of SAM35, SAM40, SAM40X3 had non-optimal elemental compositions, and were produced with non-optimal thermal spray parameters (powder size, gun pressure, and particle velocity), and exhibited light rusting after 13 cycles in the classic salt fog test. However, optimized elemental compositions of these Fe-based amorphous metals in the form of fully dense pore-free material have shown no corrosion after 24 cycles in this aggressive test. Promising formulations at the present time are believed to be SAM2X5 and SAM1651. Salt-fog testing of HVOF coatings of these materials showed no corrosion after more than 30 cycles (and up to 54 cycles) in the salt fog test. Such performance cannot be achieved with thermally sprayed Type 316L stainless steel, as this material loses most of its desirable corrosion-resistance during the thermal spray process. To a lesser extent, similar difficulties are encountered during the thermal spraying of Alloy C-22.

The second hypothesis tested was that amorphous metals can have better corrosion resistance than comparable, crystalline materials. It is generally believed that the corrosion resistance of amorphous metals is enhanced by the absence of precipitated intermetallic phases which deplete the matrix of those alloying elements responsible for passivity, a large number of grain boundaries intersecting the surface, and passive films with a large number of resulting defects. Defects would be expected to evolve as the passive film grows on an interface with various crystalline faces to the environment. Parts of this hypothesis have been tested by intentionally inducing devitrification in an amorphous metal, known to have good corrosion resistance in the non-crystalline state. Melt-spun ribbons of SAM2X5 and SAM40, the master alloy, were intentionally devitrified by heat treating them at various temperatures for one hour, including levels known to be above the measured crystallization temperature. The samples heat treated for one hour at 800°C, a temperature well above the crystallization temperatures of SAM2X5 and SAM40, showed a dramatic loss of corrosion resistance in comparison to the as-received samples. It has therefore been proven that such heat treatments and the resultant crystalline phase formation is deleterious to corrosion resistance. Crystalline phase correlated with poor corrosion performance include ferrite.

Furthermore, ingots and melt-spun ribbons of the Fe-based amorphous metals without grain boundaries have shown more corrosion resistance in than crystalline Alloy C-22. It has also been found that it is not been possible to render Alloy C-22 as thermal spray coating with the same corrosion resistance as the wrought alloy, though such possibilities do exist with some of the Fe-based amorphous metal formulations discussed here.

The crystalline structure of powders can vary with particle size, since different cooling rates are experienced by particles with different sizes. Particle size sensitivity is explored in this publication, in regard to the residual crystalline phases present in powders and coatings, as well as in regard to the impact of those crystalline phases on the corrosion resistance of coatings. Corrosion resistance of the SAM1651 amorphous metal alloy is discussed elsewhere [1].

It has been shown that these novel ultra-hard corrosion-resistant materials can be produced as either bulk alloys or coatings. For example, melt spinning and arc melting with drop casting can be used to render these materials as fully dense pore-free bulk alloys. Coatings can be produced with advanced thermal spray processes, or by physical vapor deposition processes such as magnetron sputtering or electron-beam evaporation. The materials can also be rendered as bulk alloys by using HVOF to form large plates on a flat mandrel. Near theoretical density has been achieved through precise control of powder size with atomization and classification.

ACKNOWLEDGMENTS

Work was sponsored by the United States Department of Energy (DOE), Office of Civilian and Radioactive Waste Management (OCRWM); and Defense Advanced Research Projects Agency (DARPA), Defense Science Office (DSO). This work was done under the auspices of the U.S. DOE by UC, Lawrence Livermore National Laboratory under Contract No. W-7405-Eng-48.
The guidance of Leo Christodoulou at DARPA DSO and of Jeffrey Walker at DOE OCRWM is gratefully acknowledged. Thermal spray SAM2X5 coatings used in this investigation were produced by Plasma Tech Incorporated (PTI) in Torrance, California, with amorphous metal powders produced by The NanoSteel Company (TNC).

REFERENCES

1. J. C. Farmer, J. J. Haslam, S. D. Day, T. Lian, R. Rebak, N. Yang, L. Aprigliano, Corrosion Resistance of Iron-Based Amorphous Metal Coatings, Proceedings of ASME PVP: Pressure Vessels & Piping (PVP) Division Conference, July 23-27, 2006 Vancouver, British Colombia, American Society of Mechanical Engineers, PVP2006-ICPVT11-93835, New York, NY 7 p. (2006).
2. J. C. Farmer, J. J. Haslam, S. D. Day, D. J. Branagan, C. A. Blue, J. D. K. Rivard, L. F. Aprigliano, N. Yang, J. H. Perepezko, M. B. Beardsley, Corrosion Characterization of Iron-Based High-Performance Amorphous-Metal Thermal-Spray Coatings, PVP2005-71664, Proceedings of ASME PVP: Pressure Vessels & Piping Division Conference, Grand Hyatt, Denver, Colorado, July 17-21, 2005, American Society of Mechanical Engineers, Three Park Avenue, New York, New York, 7 pages (2005).
3. J. C. Farmer, J. J. Haslam, S. D. Day, D. J. Branagan, M. C. Marshall, B. E. Mecham, E. J. Buffa, C. A. Bue, J. D. K. Rivard, D. C. Harper, M. B. Beardsley, D. T. Weaver, L. F. Aprigliano, L. Kohler, R. Bayles, E. J. Lemieux, T. M. Wolejsza, N. Yang, G. Lucadamo, J. H. Perepezko, K. Hildal, L. Kaufman, A. H. Heuere, F. Ernst, G. M. Michal, H. Kahn, E. J. Lavernia, High-Performance Corrosion-Resistant Materials: Iron-Based Amorphous-Metal Thermal-Spray Coatings, High-Performance Corrosion-Resistant Materials (HPCRM) Annual Report, UCRL-TR-206717, Lawrence Livermore National Laboratory, Livermore, California, 178 pages, September 28 (2004).
4. F. Guo, S. J. Poon, G. J. Shiflet, Metallic Glass Ingots Based on Yttrium, Applied Physics Letters, Vol. 83, No. 13, pp. 2575-2577 (2003).
5. Z. P. Lu, C. T. Liu, W. D. Porter, Role of Yttrium in Glass Formation of Fe-Based Bulk Metallic Glasses, Vol. 83, No. 13, Applied Physics Letters, pp. 2581-2583 (2003).
6. V. Ponnambalam, S. J. Poon and G. Shiflet, J. Mater. Res., 19 (5), 1320, 2004.

7. D. J. Branagan, M. C. Marshall, B. E. Mecham, L. F. Aprigliano, R. Bayles, E. J. Lemieux, T. M. Wolejsza, F. J. Martin, J. C. Farmer, J. J. Haslam, S. D. Day, Wear and Corrosion Resistant Amorphous / Nanostructured Steel Coatings for Replacement of Electrolytic Hard Chromium, UCRL Report, Lawrence Livermore National Laboratory, Livermore, California. 7 pages (2005); Proceedings of the International Thermal Spray Conference and Exposition, American Society of Materials International, Seattle, Washington, May 15-18, 2006 (2006).
8. D. J. Branagan, Method of Modifying Iron-Based Glasses to Increase Crystallization Temperature without Changing Melting Temperature, United States Patent Application No. 20040250929, Filed December 16, 2004.
9. D. J. Branagan, Properties of Amorphous/Partially Crystalline Coatings, United States Patent Application No. 20040253381, Filed December 16, 2004.
10. D. J. Branagan, Methods of Forming Hardened Surfaces, United States Patent No. 6,767,419, Filed November 9, 2000, Granted July 27, 2004.
11. D. J. Branagan, Method for Protecting a Surface, United States Patent Application 20040140021, Filed July 22, 2004.
12. D. J. Branagan, Joseph V. Burch, Methods of Forming Steel, United States Patent No. 6,258,185, Filed May 25, 1999, Granted July 10, 2001.
13. D. Chidambaram, C. R. Clayton, M. R. Dorfman, Evaluation of the Electrochemical Behavior of HVOF-Sprayed Alloy Coatings, Surface and Coatings Technology, Vol. 176, pp. 307-317 (2004).
14. D. E. Polk, B. C. Giessen, Overview of Principles and Applications, Chapter 1, pp. 2-35, Metallic Glasses, J. J. Gilman, H. J. Leamy, Eds., American Society of Metals, Metals Park, Ohio, 348 p. (1978).
15. R. M. Latanison, Corrosion Resistance of Metastable Alloys Processed by Rapid Solidification, Workshop on Amorphous Metals and Semiconductors, Electric Power Research Institute (EPRI), May 12-18, 1985 (1985).
16. J. R. Scully, A. Gerbert, J. H. Payer, Corrosion and Related Mechanical Properties of Bulk Metallic Glasses, Journal of Materials Research, submitted for publication (2006).
17. K. Kishitake, H. Era, F. Otsubo, Characterization of Plasma Sprayed Fe-10Cr-10Mo-(C,B) Amorphous Coatings, Vol. 5, No. 2, pp. 145-153 (1996).
18. S. Pang, T. Zhang, K. Asami, A. Inoue, Materials Transactions, Effects of Chromium on the Glass Formation and Corrosion Behavior of Bulk Glassy Fe-Cr-Mo-C-B Alloys, Vol. 43, No. 8, pp. 2137-2142 (2002).
19. S. J. Pang, T. Zhang, K. Asami, A. Inoue, Synthesis of Fe-Cr-Mo-C-B-P Bulk Metallic Glasses with High Corrosion Resistance, Acta Materialia, Vol. 50, pp. 489-497 (2002).
20. H. Shinimiya, A. Nakazawa, Z. Kato, A. A. El Moneium, Y. Niizeki, K. Asami, K. Hashimoto, Corrosion Resistant Bulk Amrophous Ni-Cr-Ta-Mo-Nb-5P Alloys in Concentrated Hydrochloric Acids, Paper 319, Session on Corrosion and Electrochemistry of Advanced Materials in Honor of Koji Hashimoto, 208th Meeting of the Electrochemical Society, Westing Bonaventure Hotel, Los Angeles, California, October 16-21, 2005, Electrochemical Society, Pennington, New Jersey (2005).
21. J. E. Harrar, J. F. Carley, W. F. Isherwood, E. Raber, Report of the Committee to Review the Use of J-13 Well Water in Nevada Nuclear Waste Storage Investigations, Yucca Mountain Project, UCID-21867, Lawrence Livermore National Laboratory, Livermore, California, 111 pages (1990).

22. H. P. Hack, Crevice Corrosion Behavior of Molybdenum-Containing Stainless Steel in Seawater, Materials Performance, Vol. 22, No. 6, pp. 24–30 (1983).
23. K. A. Gruss, G. A. Cragnolino, D. S. Dunn, N. Sridar, Repassivation Potential for Localized Corrosion of Alloys 625 and C22 in Simulated Repository Environments, Paper 149, Corrosion 98, National Association of Corrosion Engineers, Houston, TX, 9 pages (1998).
24. A. I. Asphahani, Corrosion Resistance of High Performance Alloys, Materials Performance, Vol. 19, No. 12, pp. 33–43 (1980).
25. C. K. Saw, X-ray Scattering Techniques for Characterization Tools in the Life Sciences, Nanotechnologies for the Life Science, Edited by Challa Kumar, Wiley-VCH Verlag GmbH & Co., KGaA, Weinheim (2006).
26. C. K. Saw and R. B. Schwarz, Chemical Short-Range Order in Dense Random-Packed Models", Journal of the Less-Common Metals, 140, 385-393 (1988).
27. J. R. Scully, J. L. Hudson, T. Lunt, G. Ilevbare, B. Kehler, Localized Corrosion Initiation and Transition to Stabilization in Alloys 625 and C-22, Final Report, TRW/DOE YMP Purchase Order Number A10762JM8A, September 30, 1999, 27 pages (1999).
28. Standard Practice for Conventions Applicable to Electrochemical Measurements in Corrosion Testing, Designation G 3-89, 1997 Annual Book of American Society for Testing and Materials (ASTM) Standards, Section 3, Vol. 3.02, pp. 36–44 (1997).
29. Standard Reference Test Method for Making Potentiostatic and Potentiodynamic Anodic Polarization Measurements, Designation G 5-94, 1997 Annual Book of American Society for Testing and Materials (ASTM) Standards, Section 3, Vol. 3.02, pp. 54–57 (1997).
30. Standard Reference Test Method for Making Potentiostatic and Potentiodynamic Anodic Polarization Measurements, Designation G 5-87, 1989 Annual Book of American Society for Testing and Materials (ASTM) Standards, Section 3, Vol. 3.02, pp. 79–85 (1989).
31. Standard Test Method for conducting Cyclic Potentiodynamic Polarization Measurements for Localized Corrosion Susceptibility of Iron-, Nickel-, or Cobalt-Based Alloys, Designation G 61-86, 1997 Annual Book of American Society for Testing and Materials Standards, Section 3, Vol. 3.02, pp. 231–235 (1997).
32. W. T. Kim, K. Clay, C. Small, B. Cantor, Heat Treatment of a Melt Spun Fe70Cr18Mo2B10 Alloy, Journal of Non-Crystalline Solids, Vol. 127, pp. 273-286 (1991).
33. R. S. Treseder, R. Baboian, C. G. Munger, Polarization Resistance Method for Determining Corrosion Rates, NACE Corrosion Engineer's Reference Book, Second Edition, National Association of Corrosion Engineers, 1440 South Creek Drive, Houston, Texas, pp. 65-66 (1991).
34. D. A. Jones, Faraday's Law, Section 3.1.1, Electrochemical Kinetics of Corrosion," Chapter 3, Principles and Prevention of Corrosion, 2nd Edition, Prentice Hall, Upper Saddle River, NJ, Equations 3 and 5, pp. 75–76 (1996).
35. A. J. Bard, L. R. Faulkner, Liquid Junction Potentials, Section 2.3, Potentials and Thermodynamics of Cells, Chapter 2, Electrochemical Methods, Fundamentals and Applications, John Wiley and Sons, New York, NY, 1980, Eqn. 2.3.39, p. 71, Table 2.3.2, p. 67 (1980).

TABLES

Table 1 – The melt-spinning process was used to perform a systematic study of various elemental compositions, each based on the Fe-based DAR40 composition, with 1, 3, 5, and 7 atomic percent additions of specific elements believed to be beneficial to glass formation or corrosion resistance. Elemental additions investigated included nickel (Ni), molybdenum (Mo), yttrium (Y), titanium (Ti), zirconium (Zr) and chromium (Cr). The two formulations of greatest interest at the present time, based upon corrosion resistance and ease of processing are SAM2X5 ($Fe_{49.7}Cr_{17.7}Mn_{1.9}Mo_{7.4}W_{1.6}B_{15.2}C_{3.8}Si_{2.4}$), which has a relatively high CCR, and yttrium-containing SAM1651 ($Fe_{48.0}Cr_{15.0}Mo_{14.0}B_{6.0}C_{15.0}Y_{2.0}$), which has a relatively low CCR.

Nominal Composition in Atomic Percent - Used to Prepare Samples														
Alloy	**Specification / Formula**	**Fe**	**Cr**	**Mn**	**Mo**	**W**	**B***	**C***	**Si**	**Y**	**Ni**	**P***	**Co**	**Total**
316L	**UNS S31603**	**68.0**	**18.0**	**1.5**	**1.5**	**0.0**	**0.0**	**0.0**	**1.0**	**0.0**	**10.0**	**0.0**	**0.0**	**100**
C-22	**UNS N06022**	**4.0**	**25.0**	**0.1**	**8.0**	**1.4**	**0.0**	**0.0**	**1.0**	**0.0**	**60.0**	**0.0**	**0.5**	**100**
SAM40	**$Fe_{52.3}Mn_2Cr_{19}Mo_{2.5}W_{1.7}B_{16}C_4Si_{2.5}$**	**52.3**	**19.0**	**2.0**	**2.5**	**1.7**	**16.0**	**4.0**	**2.5**	**0.0**	**0.0**	**0.0**	**0.0**	**100**
SAM2X1	**$(SAM40)_{99} + Mo_1$**	**51.8**	**18.8**	**2.0**	**3.5**	**1.7**	**15.8**	**4.0**	**2.5**	**0.0**	**0.0**	**0.0**	**0.0**	**100**
SAM2X3	**$(SAM40)_{97} + Mo_3$**	**50.7**	**18.4**	**1.9**	**5.4**	**1.6**	**15.5**	**3.9**	**2.4**	**0.0**	**0.0**	**0.0**	**0.0**	**100**
SAM2X5	**$(SAM40)_{95} + Mo_5$**	**49.7**	**18.1**	**1.9**	**7.4**	**1.6**	**15.2**	**3.8**	**2.4**	**0.0**	**0.0**	**0.0**	**0.0**	**100**
SAM2X7	**$(SAM40)_{93} + Mo_7$**	**48.6**	**17.7**	**1.9**	**9.3**	**1.6**	**14.9**	**3.7**	**2.3**	**0.0**	**0.0**	**0.0**	**0.0**	**100**
SAM1651	**$Fe_{48}Mo_{14}Cr_{15}Y_2C_{15}B_6$**	**48.0**	**15.0**	**0.0**	**14.0**	**0.0**	**6.0**	**15.0**	**0.0**	**2.0**	**0.0**	**0.0**	**0.0**	**100**

Table 2 – The actual compositions of several samples used in this study were determined with energy dispersive X-ray spectroscopy (EDS), and are summarized here. The measurements were done for wrought samples of Type 316L stainless steel and nickel-based Alloy C-22; melt-spun ribbons of SAM40, SAM2X1, SAM2X3, SAM2X5 and SAM2X7; and a drop-cast ingot of SAM1651.

Actual Compositions in Atomic Percent - Determined by Energy Dispersive X-Ray Spectroscopy														
Alloy	**Sample**	**Fe**	**Cr**	**Mn**	**Mo**	**W**	**B***	**C***	**Si**	**Y**	**Ni**	**P***	**Co**	**Total**
316L	**MSR**	**67.6**	**18.7**	**1.3**	**1.2**	**0.0**	**0.0**	**0.0**	**1.2**	**0.0**	**10.0**	**0.0**	**0.0**	**100**
C-22	**MSR**	**3.9**	**25.2**	**0.1**	**7.8**	**1.4**	**0.0**	**0.0**	**1.1**	**0.0**	**60.0**	**0.0**	**0.5**	**100**
SAM40	**MSR**	**51.9**	**19.2**	**2.6**	**2.5**	**1.5**	**16.0**	**4.0**	**2.2**	**0.0**	**0.0**	**0.0**	**0.0**	**100**
SAM2X1	**MSR**	**52.0**	**19.1**	**2.7**	**2.9**	**1.6**	**15.8**	**4.0**	**1.9**	**0.0**	**0.0**	**0.0**	**0.0**	**100**
SAM2X3	**MSR**	**49.3**	**17.9**	**2.6**	**5.3**	**2.5**	**15.5**	**3.8**	**3.1**	**0.0**	**0.0**	**0.0**	**0.0**	**100**
SAM2X5	**MSR**	**48.8**	**17.6**	**2.4**	**7.2**	**2.5**	**15.0**	**3.7**	**2.7**	**0.0**	**0.0**	**0.0**	**0.0**	**100**
SAM2X7	**MSR**	**46.9**	**16.9**	**2.3**	**10.0**	**2.5**	**14.9**	**3.7**	**2.9**	**0.0**	**0.0**	**0.0**	**0.0**	**100**
SAM1651	**Ingot**	**49.1**	**14.6**	**0.0**	**13.9**	**0.0**	**5.9**	**14.0**	**0.3**	**1.9**	**0.2**	**0.0**	**0.0**	**100**

Table 3 – Thermal analysis data (DTA or DSC) for Fe-based glass forming alloys suitable for thermal spray deposition as summarized in this table. The two formulations of greatest interest at the present time are SAM2X5 ($Fe_{49.7}Cr_{17.7}Mn_{1.9}Mo_{7.4}W_{1.6}B_{15.2}C_{3.8}Si_{2.4}$), which has a relatively high CCR, and yttrium-containing SAM1651 ($Fe_{48.0}Cr_{15.0}Mo_{14.0}B_{6.0}C_{15.0}Y_{2.0}$), which has a relatively low CCR. These selections are based upon their good corrosion resistance and relative ease or processing.

Alloy	**T_g (°C)**	**T_x (°C)**	**T_m (°C)**	**T_L (°C)**	**T_{rg}**
SAM40	**568-574**	**623**	**1110**	**1338**	**0.53**
SAM2X1	**575**	**620**	**1124**	**1190-1210**	**0.57**
SAM2X3	**578**	**626**	**1131**	**1190-1210**	**0.57**
SAM2X5	**579**	**628**	**1133**	**1190-1210**	**0.57**
SAM2X7	**573**	**630**	**1137**	**1190-1210**	**0.57**
SAM1651	**584**	**653**	**1121**	**1290**	**0.55**

Table 4 – Measurements of the micro-hardness of Fe-based amorphous metal thermal spray coatings.

	Measured Vickers Micro-Hardness (kg mm^{-2})	
Loading Conditions	**As-Sprayed HVOF-Coating**	**Devitrified at 700°C for 10 Minutes**
HV100 (100-gram load)	**1050-1200**	**1300-1500**
HV300 (300-gram load)	**1000-1100**	**1200-1350**

Table 5 – The conversion of the corrosion current density to penetration rate (corrosion rate) requires the parameters summarized in this table. These penetration rates are for an assumed current density of one microamp per square centimeter (1 μA cm^{-2}). If the corrosion rate is 2 μA cm^{-2} instead of the assumed 1 μA cm^{-2}, the penetration rate is simply doubled. The value of Faraday's constant (F) is 96,484.6 C $equiv^{-1}$.

Alloy	ρ_{alloy}	$n_{alloy} = (f_j n_j / a_j)/100$		$(dp/dt) = (i_{corr})/(\rho_{alloy} \times n_{alloy} \times F)$			
	g cm^{-3}			**cm sec^{-1}**		**μm $year^{-1}$**	
		Low	**High**	**Low**	**High**	**Low**	**High**
316L SS	**7.85**	**3.9049E-02**	**6.5291E-02**	**2.0222E-11**	**3.3811E-11**	**6.3772**	**10.6627**
C-22	**8.69**	**3.8041E-02**	**6.7509E-02**	**1.7667E-11**	**3.1352E-11**	**5.5714**	**9.8872**
SAM2X5	**7.65**	**5.4149E-02**	**7.9309E-02**	**1.7083E-11**	**2.5020E-11**	**5.3872**	**7.8904**
SAM1651	**6.18**	**4.6979E-02**	**8.0221E-02**	**2.0906E-11**	**3.5699E-11**	**6.5928**	**11.2579**

Table 6 – A description of the standard GM9540P Salt Fog Test is summarized here. Note that the salt solution mists (denoted with asterisks) consisted of 1.25% solution containing 0.9% sodium chloride, 0.1% calcium chloride, and 0.25% sodium bicarbonate.

24-Hour Test Cycle for GM9540P Accelerated Corrosion Test		
Shift	**Elapsed Time (hrs)**	**Event**
Ambient Soak	**0**	**Salt solution mist for 30 seconds, followed by ambient exposure at 13-28°C (55-82°F)**
	1.5	**Salt solution mist for 30 seconds, followed by ambient exposure at 13-28°C (55-82°F)**
	3	**Salt solution mist for 30 seconds, followed by ambient exposure at 13-28°C (55-82°F)**
	4.5	**Salt solution mist for 30 seconds, followed by ambient exposure at 13-28°C (55-82°F)**
Wet Soak	**8 to 16**	**High humidity exposure for 8 hours at 49 ± 0.5°C (120 ± 1°F) and 100% RH, including a 55-minute ramp to wet conditions**
Dry Soak	**16 to 24**	**Elevated dry exposure for 8 hours at 60 ± 0.5°C (140 ± 1°F) and less than 30% RH, including a 175-minute ramp to dry conditions**

Table 7 – Values of the polarization resistance, corrosion current density, and corrosion rate, measured with linear polarization, are summarized for HVOF coatings of SAM2X5 and Alloy C-22, as well as wrought samples of Alloy C-22.

Sample	Parameter	E_{corr}	R_p	i_{corr}	dp/dt
		mV	ohms cm²	A/cm²	μm/yr
30°C Seawater					
HVOF SAM2X5	Average	-87.4	1.633E+06	2.27E-08	0.1789
HVOF SAM2X5	Standard Deviation	5.7	1.366E+06	1.36E-08	0.1071
Wrought Alloy C-22	Average	-163.2	2.744E+06	9.12E-09	0.0901
Wrought Alloy C-22	Standard Deviation	1.5	9.126E+04	3.02E-10	0.0030
Wrought Alloy C-22	Average	-312.4	6.229E+07	5.07E-09	0.0501
Wrought Alloy C-22	Standard Deviation	3.0	1.020E+08	4.40E-09	0.0435
90°C Seawater					
HVOF SAM2X5	Average	-241.0	1.255E+05	2.00E-07	1.580
HVOF SAM2X5	Standard Deviation	7.2	1.036E+04	1.73E-08	0.137
Wrought Alloy C-22	Average	-318.9	7.685E+04	3.25E-07	3.216
Wrought Alloy C-22	Standard Deviation	0.8	4.950E+02	2.10E-09	0.021
Wrought Alloy C-22	Average	-340.1	7.727E+04	3.24E-07	3.199
Wrought Alloy C-22	Standard Deviation	0.2	1.030E+03	4.29E-09	0.042
Wrought Alloy C-22	Average	-318.2	2.033E+05	1.23E-07	1.216
Wrought Alloy C-22	Standard Deviation	0.7	9.074E+02	5.50E-10	0.005
105°C 5M $CaCl_2$					
HVOF SAM2X5	Average	-240.9	7.32E+04	3.42E-07	2.696
HVOF SAM2X5	Standard Deviation	1.8	1.03E+03	4.76E-09	0.038
Wrought Alloy C-22	Average	-464.3	4.93E+04	5.10E-07	5.040
Wrought Alloy C-22	Standard Deviation	3.0	4.14E+03	4.37E-08	0.433
HVOF Alloy C-22	Average	-347.9	2.14E+03	1.17E-05	115.692
HVOF Alloy C-22	Standard Deviation	4.5	8.94E+01	4.82E-07	4.770

FIGURES

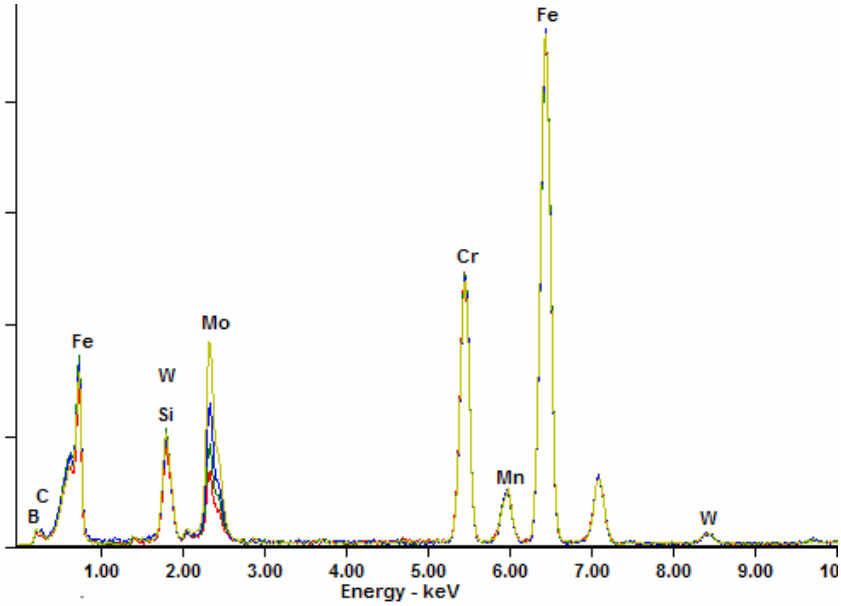

Figure 1 – This energy dispersive spectroscopy (EDS) data shows the relative abundance of molybdenum in the entire SAM2X series of iron-based amorphous metal alloys.

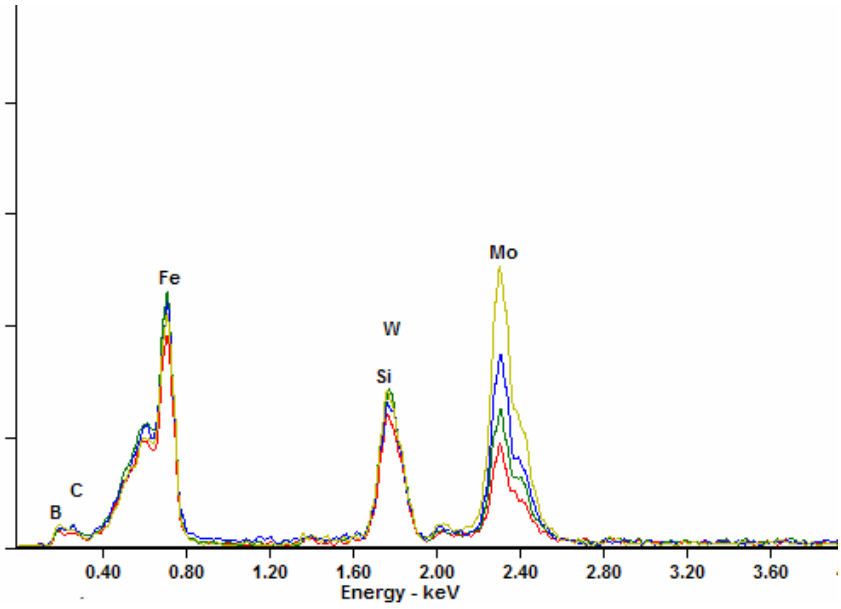

Figure 2 – This energy dispersive spectroscopy (EDS) data shows the relative abundance of molybdenum in the entire SAM2X series of iron-based amorphous metal alloys. In this case, the energy scale has been expanded, with the maximum energy being approximately four thousand electron volts, to show the molybdenum peak with greater clarity.

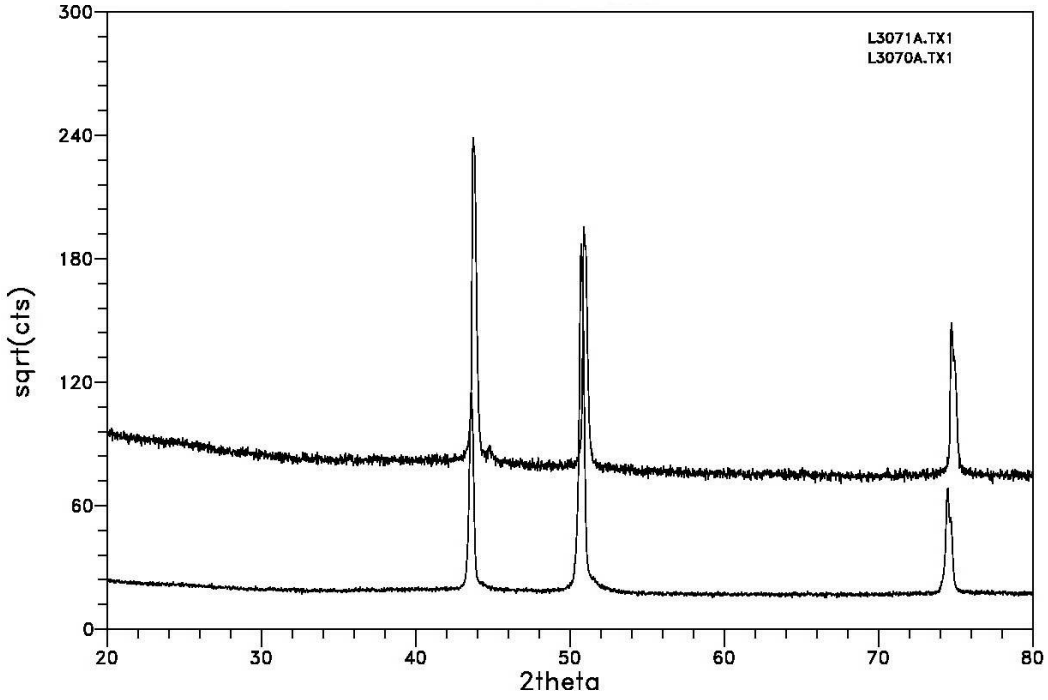

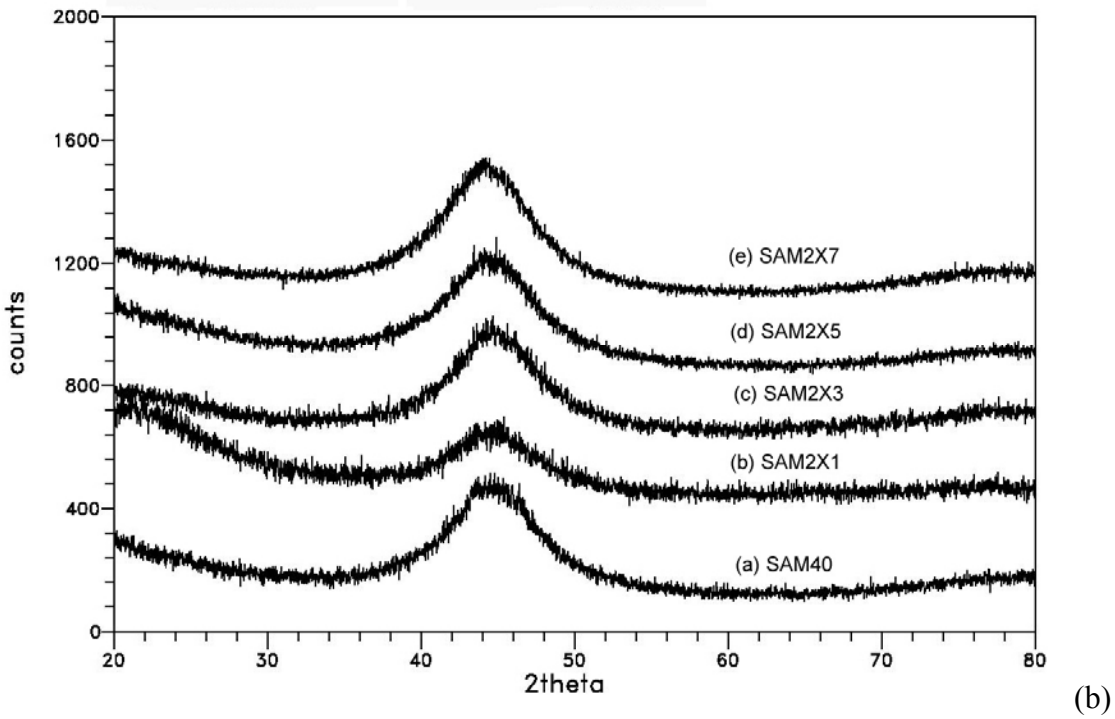

Figure 3 – (a) This figure shows X-ray diffraction data for melt-spun ribbon (MSR) samples of Type 316L stainless steel and nickel-based Alloy C-22. The strong peaks are indicative of the crystalline nature of these materials. (b) This figure shows X-ray diffraction data for melt-spun ribbon (MSR) samples of iron-based amorphous metals identified as: (a) SAM40; (b) SAM2X1; (c) SAM2X3; (d) SAM2X5; and (e) SAM2X7. All ribbons were completely amorphous.

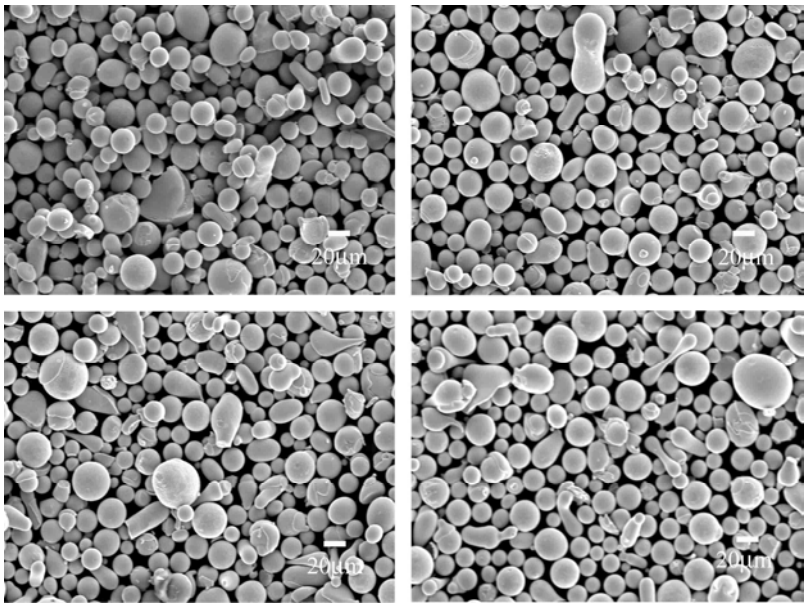

(a)

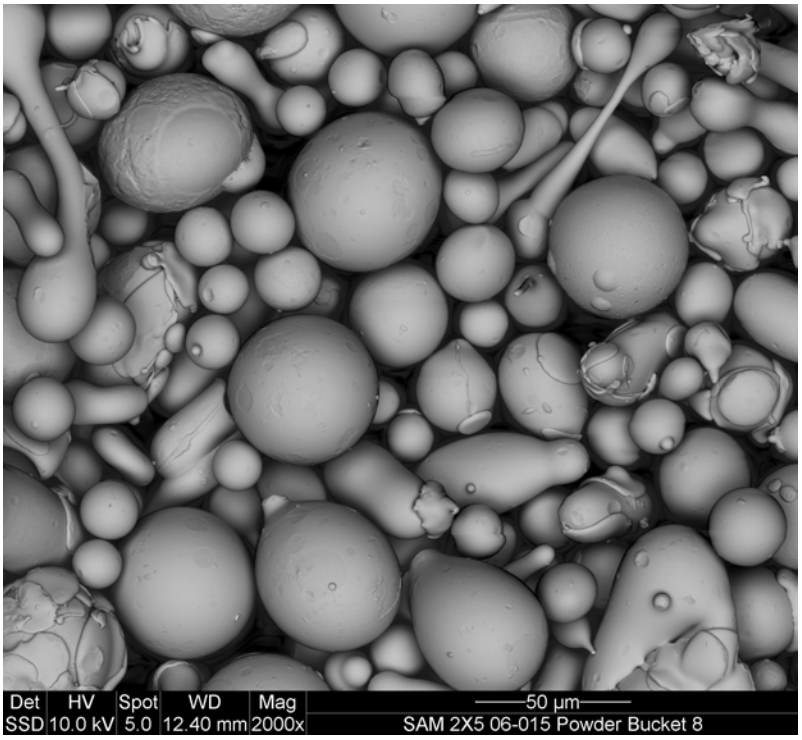

(b)

Figure 4 – Electron micrographs are shown for two lots of SAM2X5 powder produced over a span of two years: (a) Lot # 04-265; and (b) Lot # 06-123. These powders have predominantly spherical morphology, which is essential for good flow characteristics in thermal spray processes.

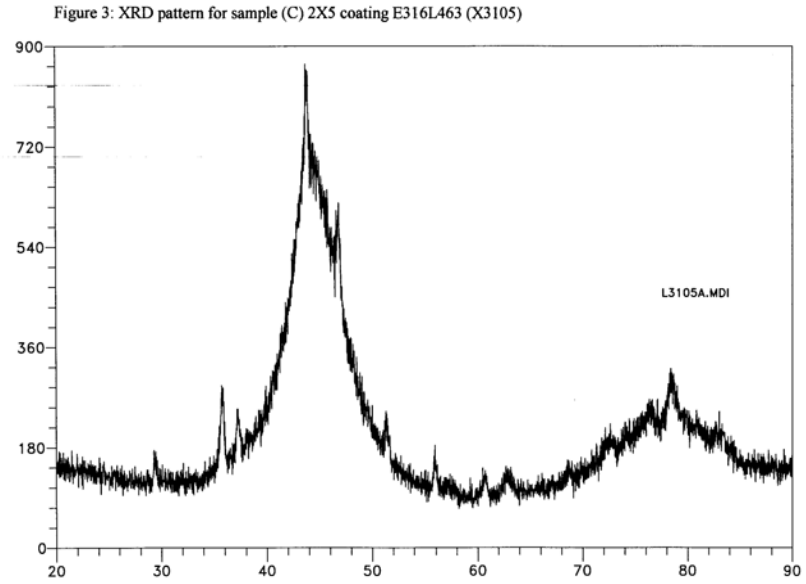

Figure 5 – XRD data (intensity verses diffraction angle 2θ) for high-velocity oxy-fuel (HVOF) coating of SAM2X5 on Type 316L stainless steel substrate prepared with JP5000 thermal spray gun. This coating was prepared with Lot #04-265 powder, which had a broad range of particle sizes (–53/+15μm).

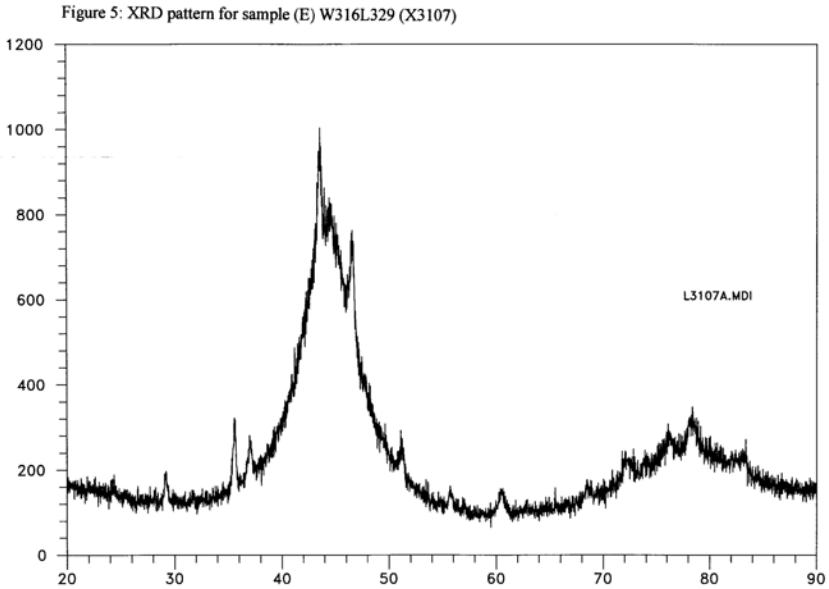

Figure 6 – XRD data (intensity verses diffraction angle 2θ) for high-velocity oxy-fuel (HVOF) coating of SAM2X5 on a Type 316L stainless steel substrate, and deposited with a JK2000 thermal-spray gun at Plasma Tech Incorporated (PTI). The feed powder was Lot # 04-200 powder, which had a relatively coarse range of particle sizes (–53/+30μm).

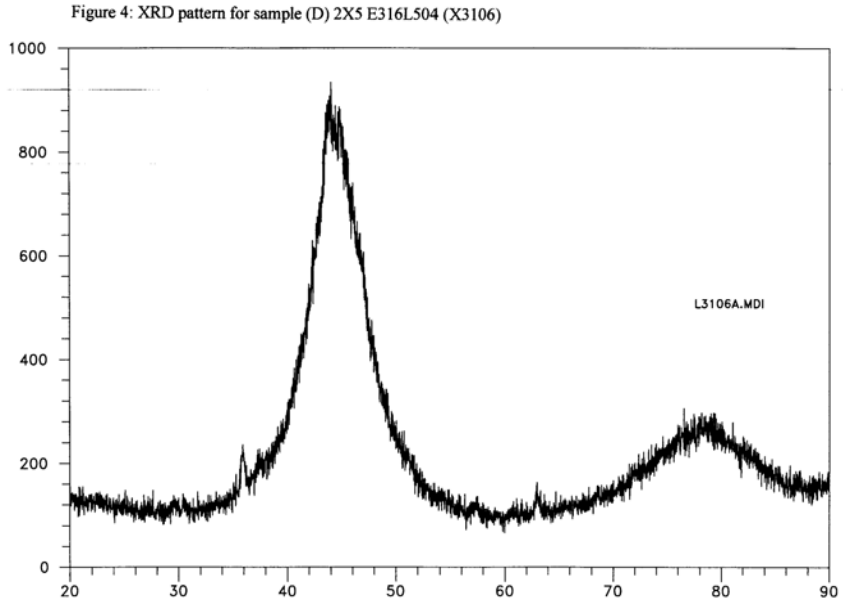

Figure 7 – XRD data (intensity verses diffraction angle 2θ) for high-velocity oxy-fuel (HVOF) coating of SAM2X5 on a Type 316L stainless steel substrate, deposited with a JK2000 thermal-spray gun at Plasma Tech Incorporated (PTI). The feed powder was Lot # 04-199 powder, which had a relatively fine range of particle sizes (–30/+15μm), and is a standard HVOF distribution.

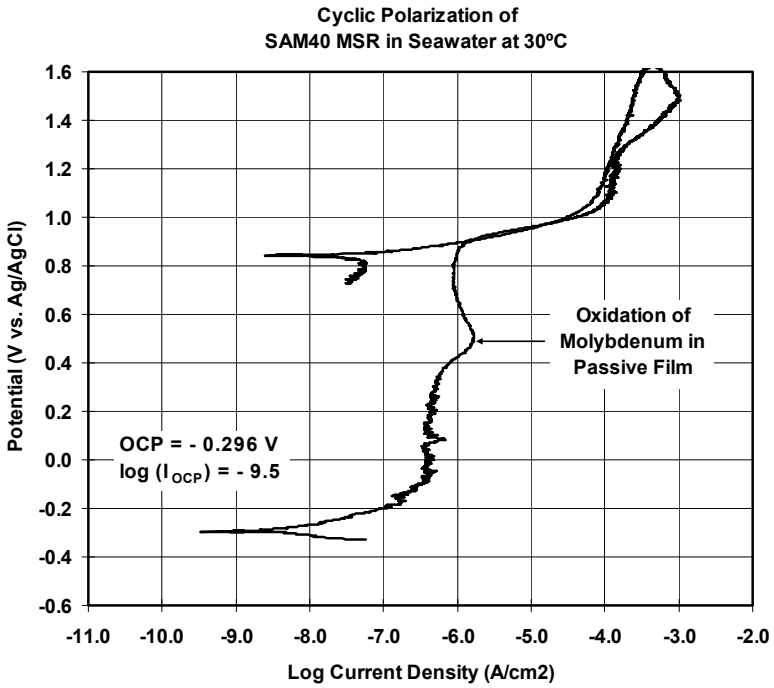

Figure 8 – This figure shows potential-current data obtained during the cyclic polarization (CP) of a SAM40 melt-spun ribbon (MSR) in natural seawater at 30°C.

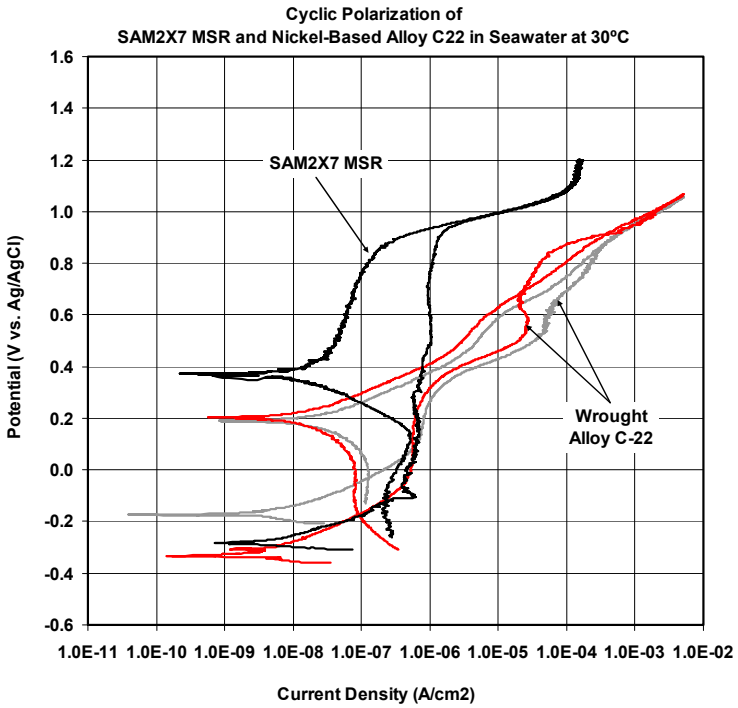

Figure 9 – This figure shows potential-current data for two wrought Alloy C-22 samples, and a SAM2X7 MSR in natural seawater at 30°C.

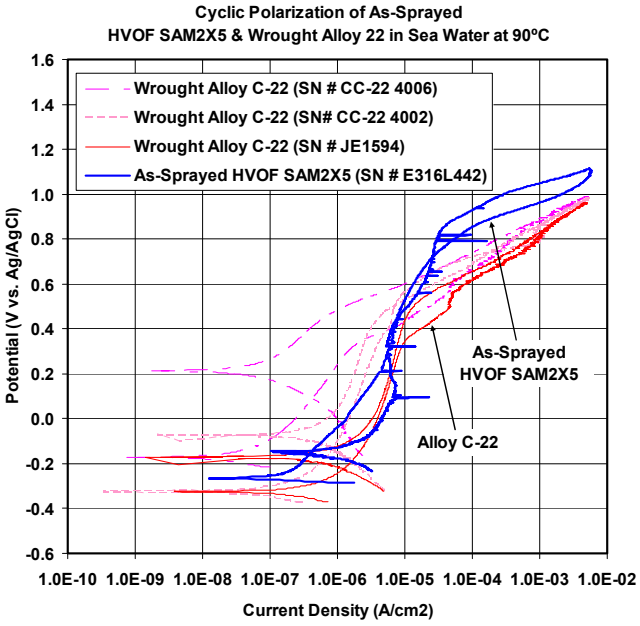

Figure 10 – This figure shows potential-current data for two wrought Alloy C-22 samples, and an as-sprayed HVOF coating of SAM2X5, which was deposited on a Type 316L stainless steel substrate, in natural seawater at 90°C.

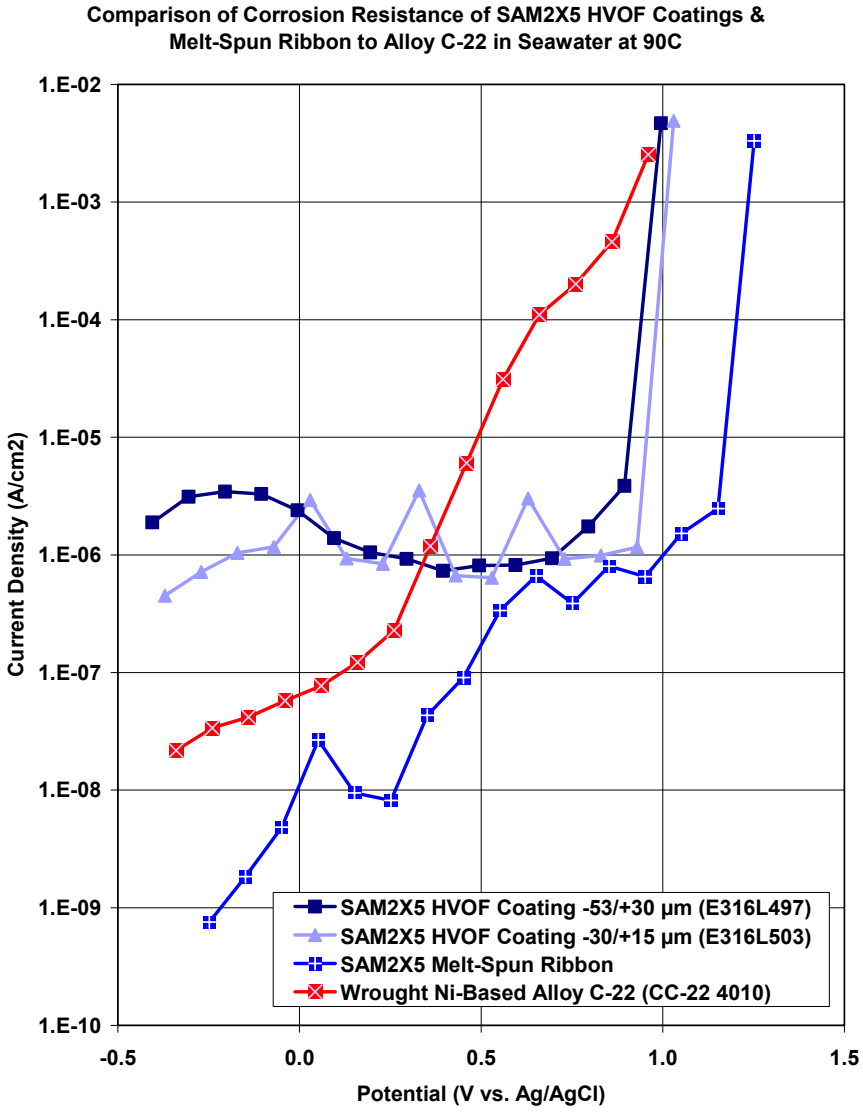

Figure 11 – Potential-step testing has been performed on wrought Alloy C-22 (reference material); fully dense and completely amorphous melt spun ribbons of SAM2X5; optimized HVOF coatings produced with –53/+30 micron powders of SAM2X5; and optimized HVOF coatings produced with –30/+15 micron powders of SAM2X5. All were tested in natural seawater heated to 90°C.

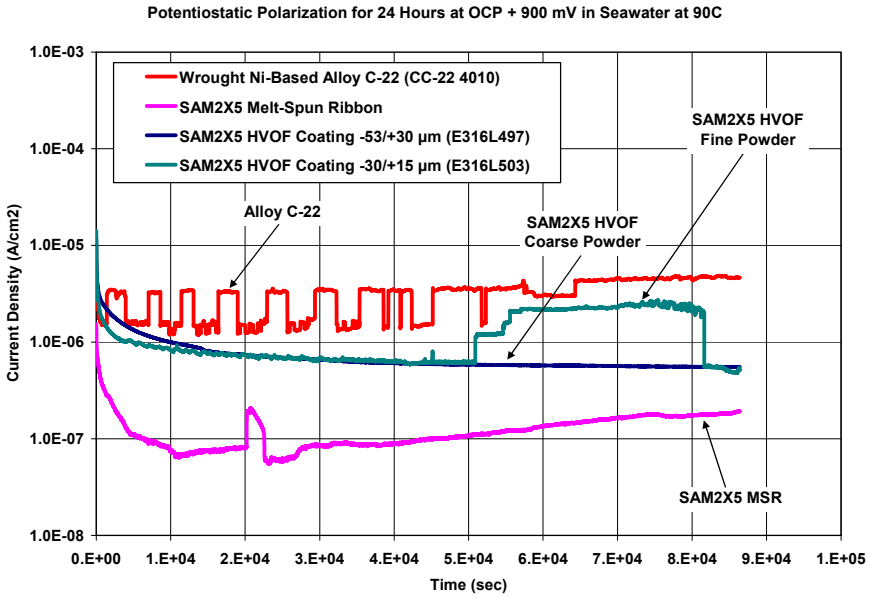

Figure 12 – Transients in current density at a constant applied potential of 900 mV verses OCP for wrought Alloy C-22 (reference material), a fully dense and completely amorphous melt spun ribbon (MSR) of SAM2X5, HVOF coatings produced with –53/+30 micron powders of SAM2X5, and HVOF coatings produced with –30/+15 micron powders of SAM2X5, all in natural seawater heated to 90°C, are compared.

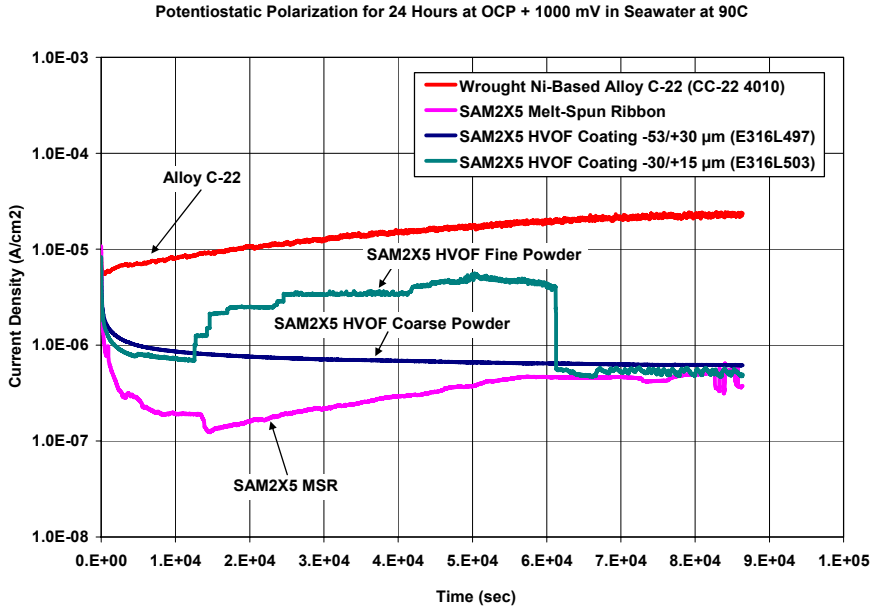

Figure 13 – Transients in current density at a constant applied potential of 1000 mV verses OCP for wrought Alloy C-22 (reference material), a fully dense and completely amorphous melt spun ribbon (MSR) of SAM2X5, HVOF coatings produced with –53/+30 micron powders of SAM2X5, and HVOF coatings produced with –30/+15 micron powders of SAM2X5, all in natural seawater heated to 90°C, are compared.

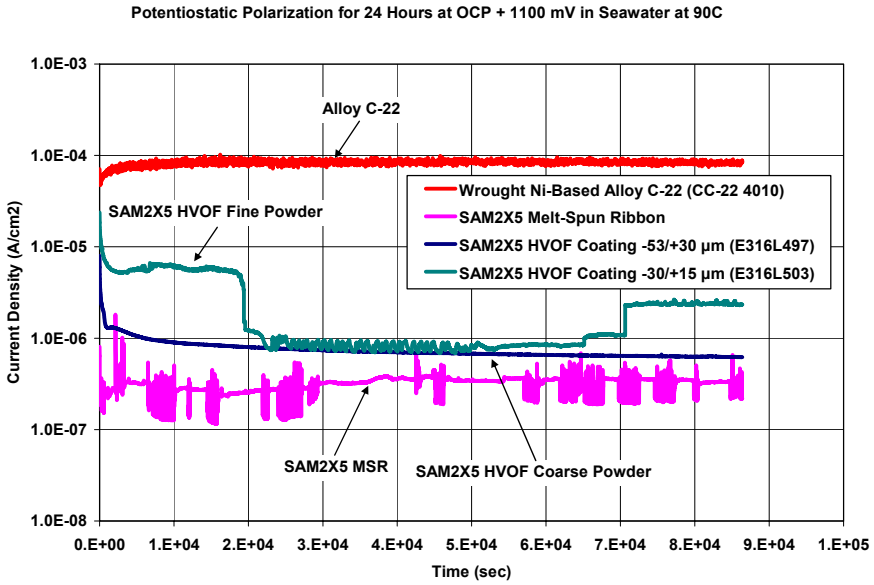

(b)

Figure 14 – Transients in current density at a constant applied potential of 1100 mV verses OCP for wrought Alloy C-22 (reference material), a fully dense and completely amorphous melt spun ribbon (MSR) of SAM2X5, HVOF coatings produced with –53/+30 micron powders of SAM2X5, and HVOF coatings produced with –30/+15 micron powders of SAM2X5, all in natural seawater heated to 90°C, are compared.

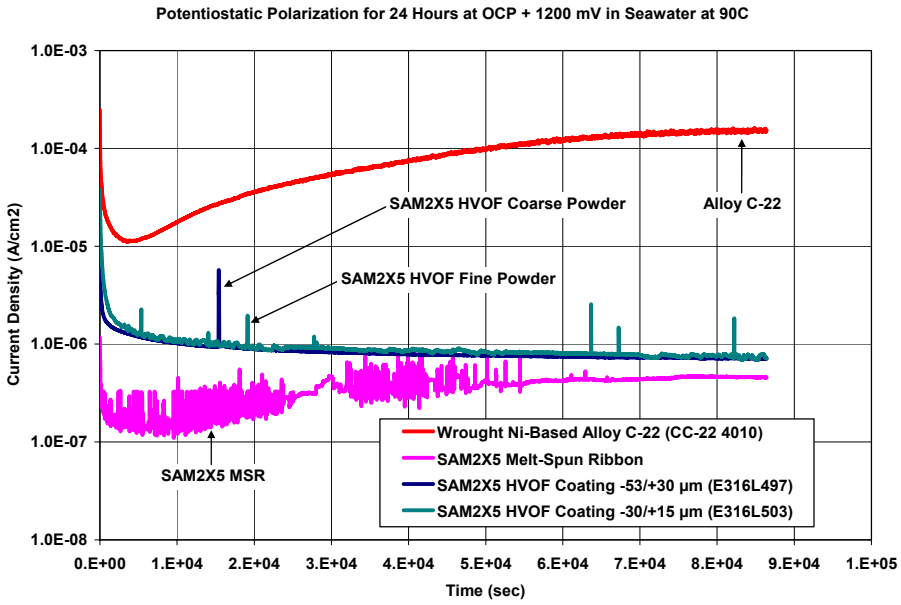

Figure 15 – Transients in current density at a constant applied potential of 1200 mV verses OCP for wrought Alloy C-22 (reference material), a fully dense and completely amorphous melt spun ribbon (MSR) of SAM2X5, HVOF coatings produced with –53/+30 micron powders of SAM2X5, and HVOF coatings produced with –30/+15 micron powders of SAM2X5, all in natural seawater heated to 90°C, are compared.

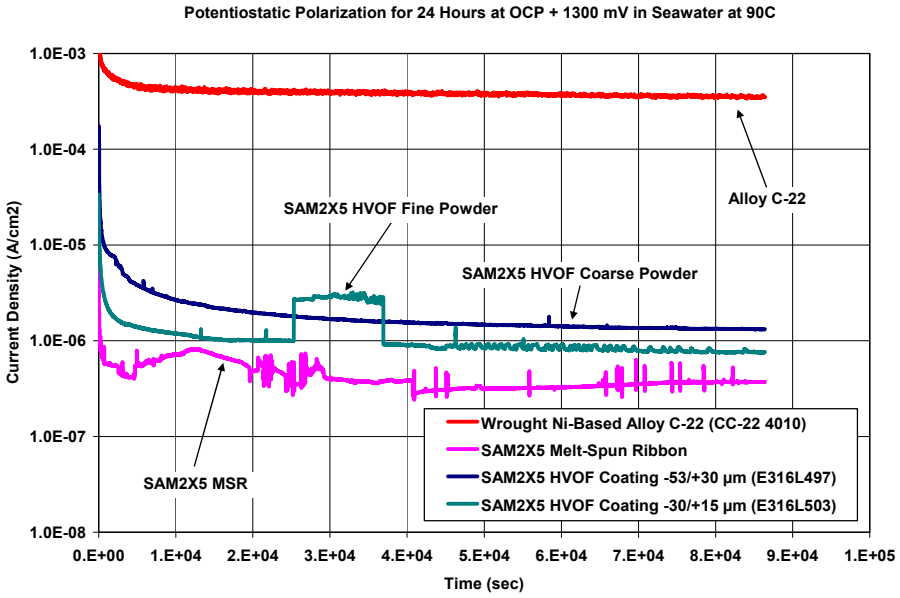

(b)

Figure 16 – Transients in current density at a constant applied potential of 1300 mV verses OCP for wrought Alloy C-22 (reference material), a fully dense and completely amorphous melt spun ribbon (MSR) of SAM2X5, HVOF coatings produced with –53/+30 micron powders of SAM2X5, and HVOF coatings produced with –30/+15 micron powders of SAM2X5, all in natural seawater heated to 90°C, are compared.

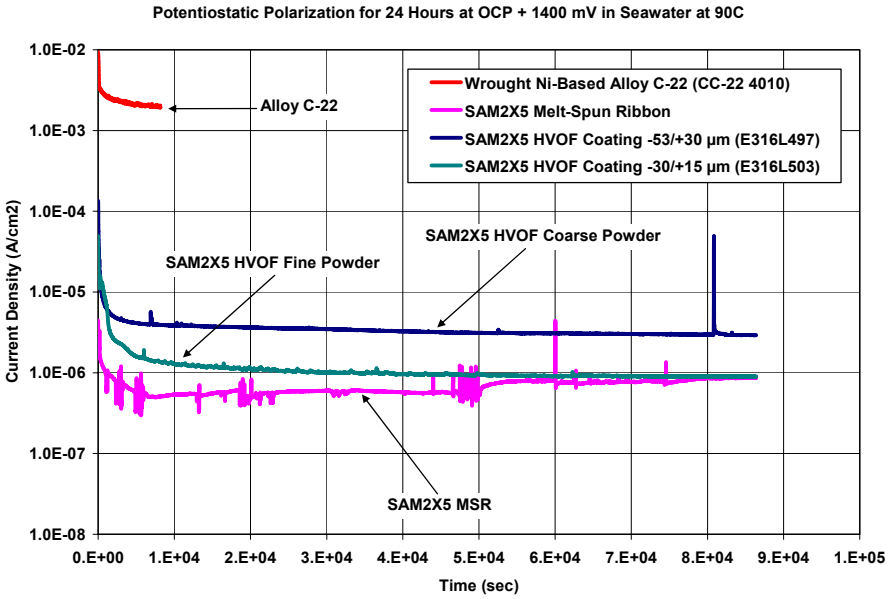

(b)

Figure 17 – Transients in current density at a constant applied potential of 1400 mV verses OCP for wrought Alloy C-22 (reference material), a fully dense and completely amorphous melt spun ribbon (MSR) of SAM2X5, HVOF coatings produced with –53/+30 micron powders of SAM2X5, and HVOF coatings produced with –30/+15 micron powders of SAM2X5, all in natural seawater heated to 90°C, are compared.

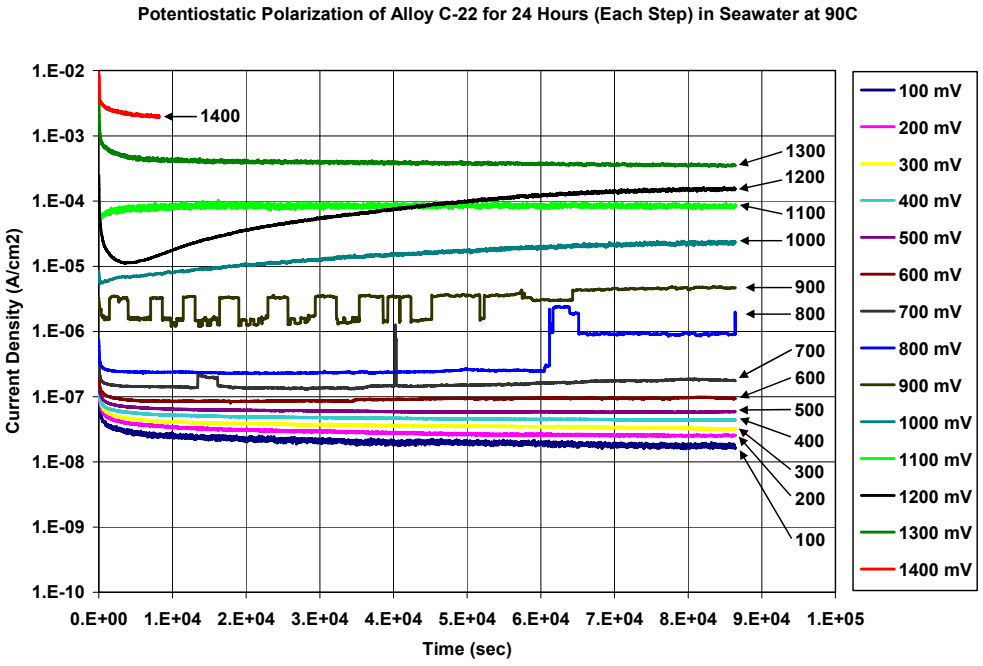

Figure 18 – Transients in current density at various levels of constant applied potential ranging from 100 to 1400 mV verses OCP for Alloy C-22 in natural seawater at 90°C. This reference material was polished to a 600-grit finish.

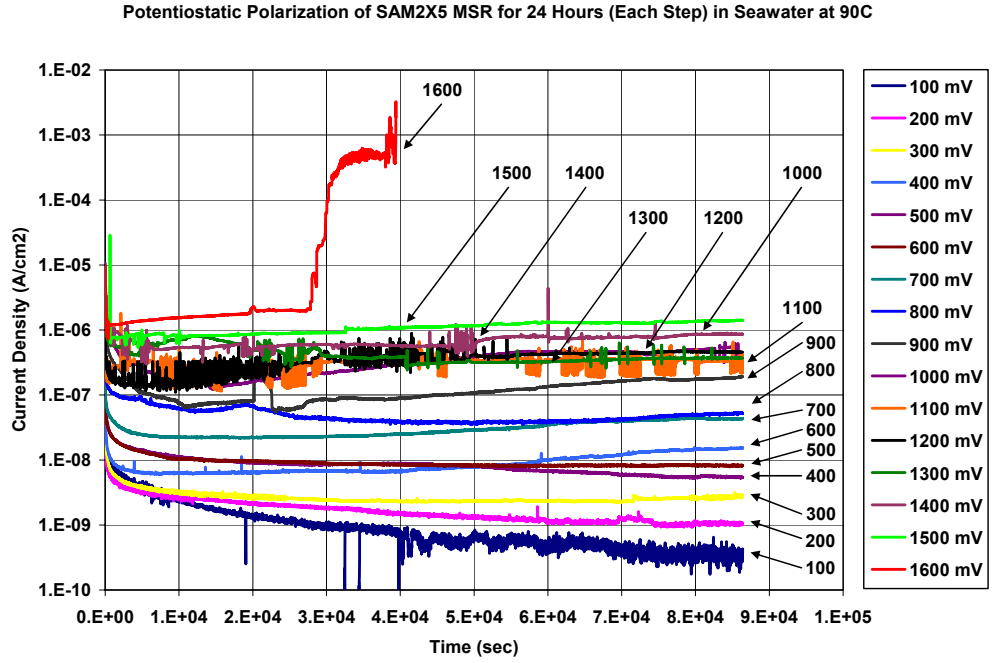

Figure 19 – Transients in current density at various levels of constant applied potential ranging from 100 to 1600 mV verses OCP for a melt-spun ribbon of SAM2X5 in natural seawater at 90°C are indicative of good passive film stability.

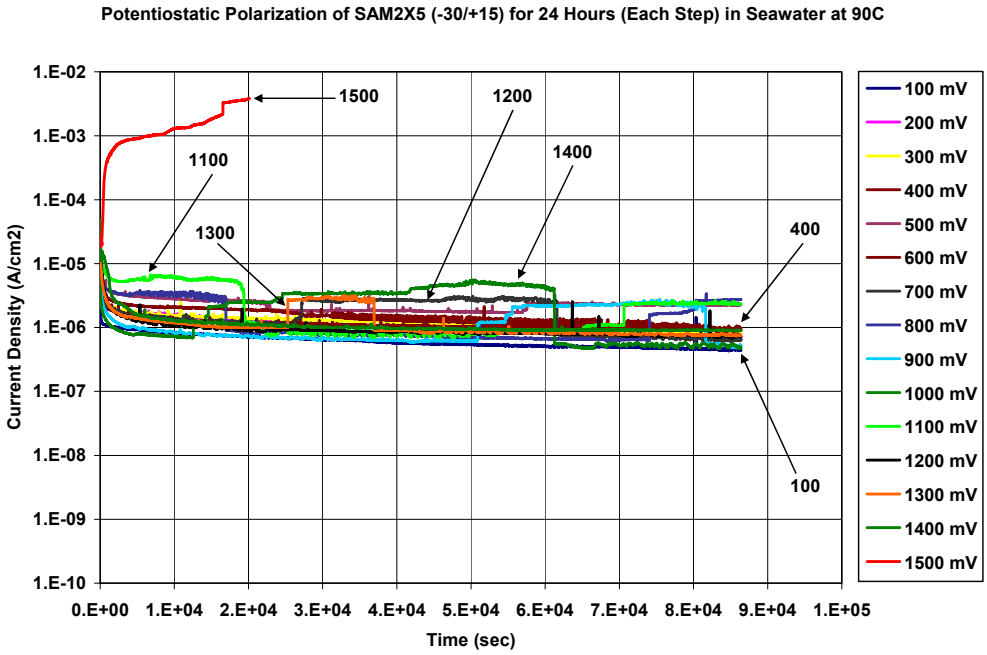

Figure 20 – Transients in current density at various levels of constant applied potential ranging from 100 to 1500 mV verses OCP for a recently optimized SAM2X5 HVOF coating (–30/+15 micron powder) in deaerated natural seawater at 90°C are indicative of good passive film stability.

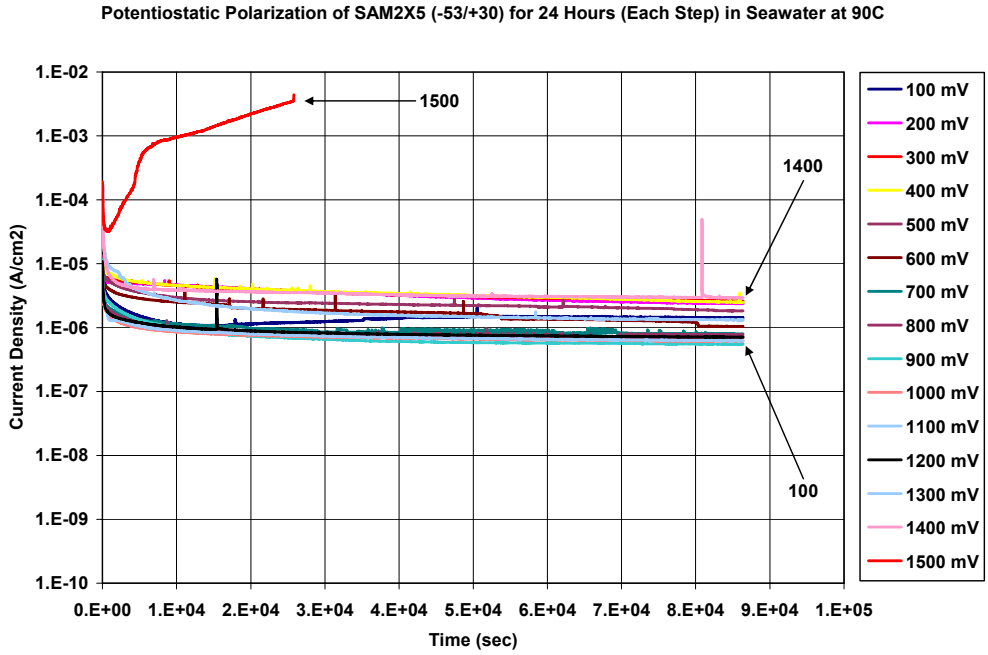

Figure 21 – Transients in current density at various levels of constant applied potential ranging from 100 to 1500 mV verses OCP for a recently optimized SAM2X5 HVOF coating (–53/+30 micron powder) in natural seawater at 90°C are indicative of exceptional passive film stability.

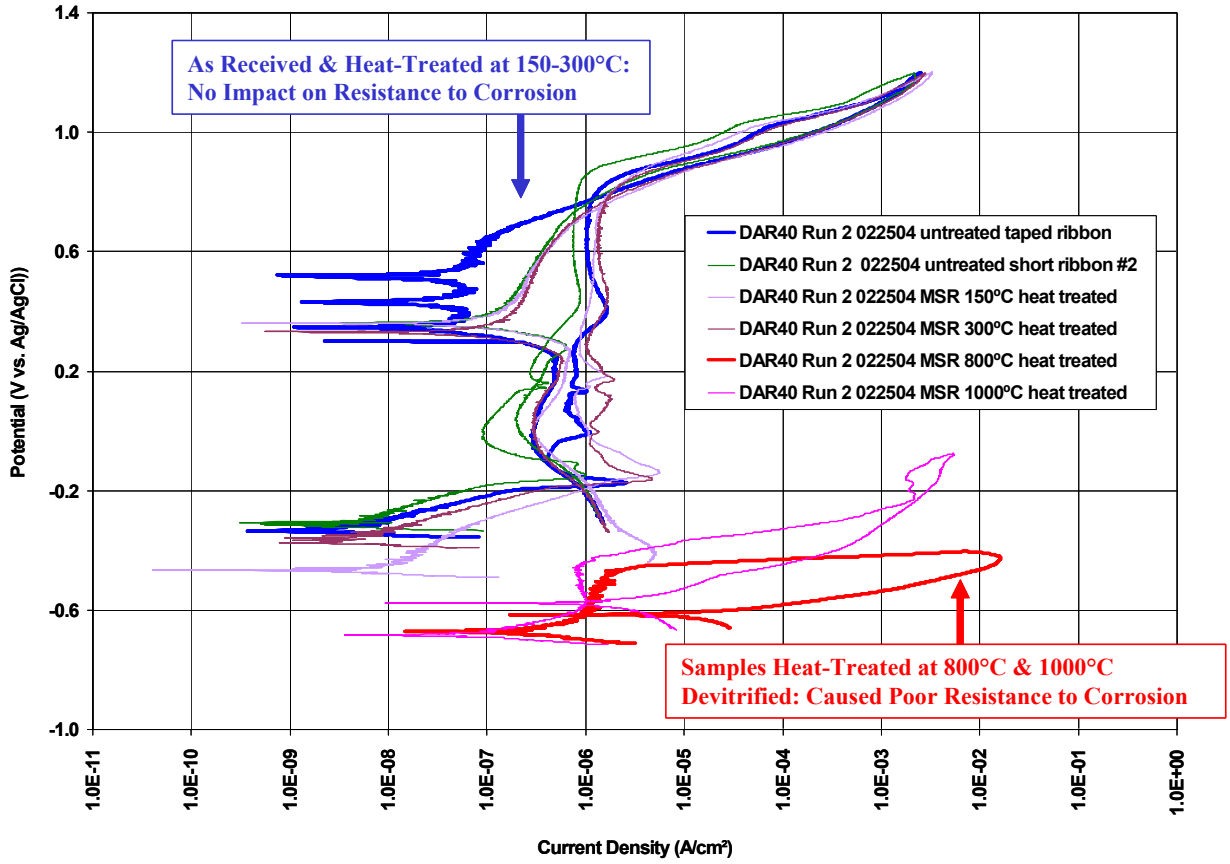

Figure 22 – To assess the sensitivity of these iron-based amorphous metals to devitrification, which can occur at very elevated temperature, melt-spun ribbon of SAM40 (also referred to as DAR40) were intentionally devitrified by heat treating them at various temperatures for one hour. After heat treatment, the samples were evaluated in low temperature seawater (30°C), to determine the impact of the heat treatment on passive film stability and corrosion resistance. The temperatures used for the heat treatment were: 150, 300, 800 and 1000°C. Untreated (as received) ribbons were also tested, and provide insight into the baseline performance. These samples showed no significant hysteresis and change in repassivation potential at heat treatments of 150-300°C, but showed a dramatic loss of corrosion resistance when heat treatments were performed at 800-1000°C, which are above the known crystallization temperature of approximately 600-650°C (623°C) given in Table 2 (Perepezko et al. 2004). Both ribbons treated at elevated temperature show large hysterisis loops, which are indicative of passive film breakdown, with a clearly defined repassivation potential near -600 mV verses Ag/AgCl (about 100 mV above the OCP). The operational limit for these materials, when being used for corrosion resistance, appears to be bounded by the recrystallization temperature.

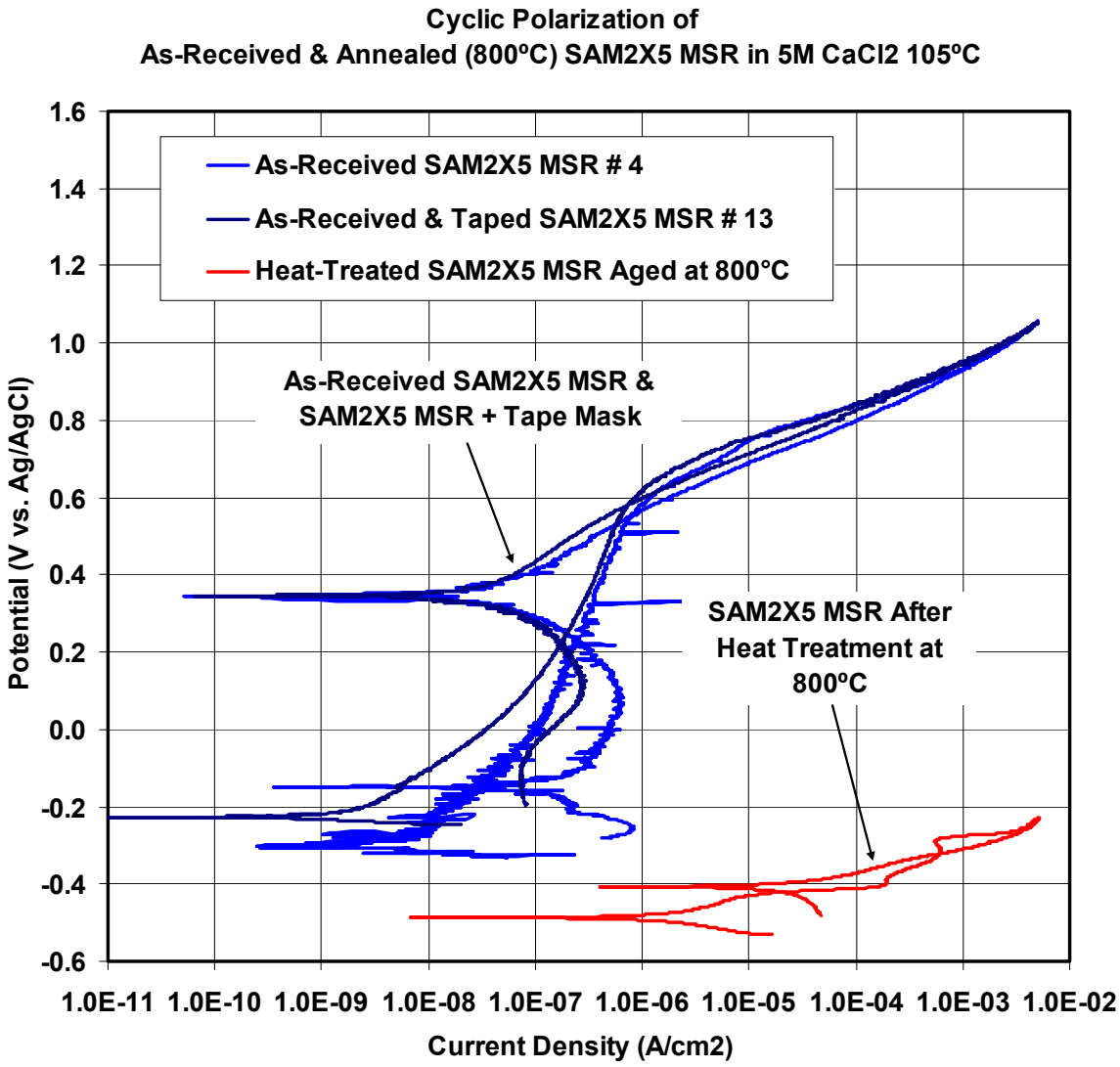

Figure 23 – Melt spun ribbons of SAM2X5 were also intentionally devitrified by heat treating at 800°C for one hour and then subjected to cyclic polarization in 5M $CaCl_2$ at 105°C. In comparison to the as-received sample, the sample heat-treated at 800C showed a dramatic loss of corrosion resistance. As discussed in regard to the preceding figure, this heat-treatment temperature was known to be above the crystallization temperature of approximately 600-650°C (623°C) given in Table 2 (Perepezko et al. 2004). The heat-treated ribbon showed a large hysterisis loop in the hot concentrated calcium chloride solution, which is indicative of passive film breakdown, with a clearly defined repassivation potential neat the OCP. The post heat-treatment microstructural characterization with electron microscopy and X-ray diffraction by Yang et al. verify the existence of a completely amorphous material below the crystallization temperature, and the development of crystalline precipitates during heat treatment above this limit. These electron microscopy images may also indicate that the corrosive attack of the precipitated crystalline phases occur to a depth of approximately 10 microns. When being used for corrosion resistance in hot geothermal brines such as calcium chloride, the operational limit also appears to be bounded by the crystallization temperature.

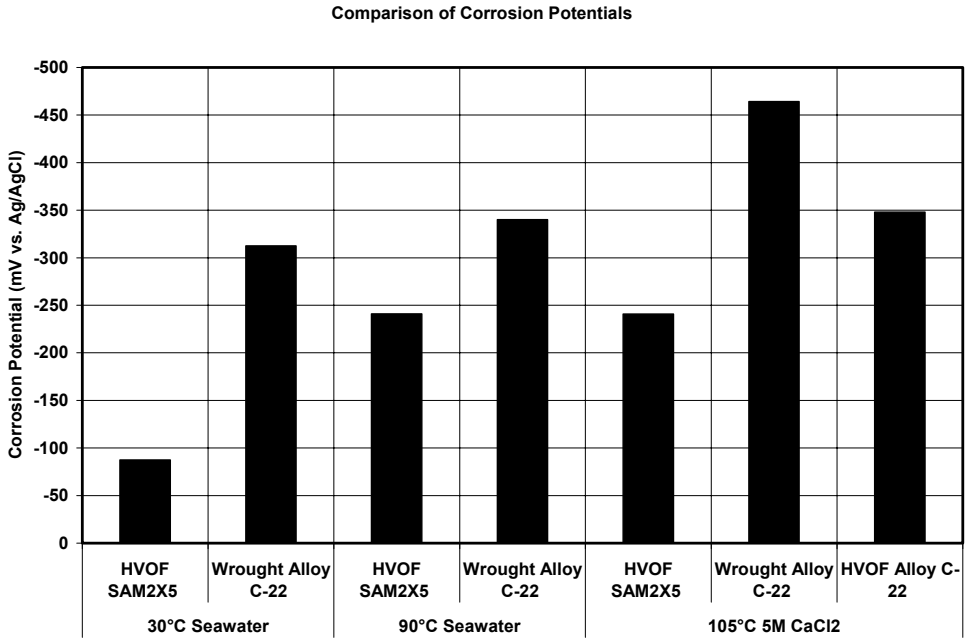

Figure 24 – The corrosion potentials for the thermal spray coatings of SAM2X5 and the reference material (wrought nickel-based Alloy C-22) in three relevant environments, natural seawater at two temperature levels, and in hot concentrated calcium chloride (5M $CaCl_2$ at 105°C) are summarized.

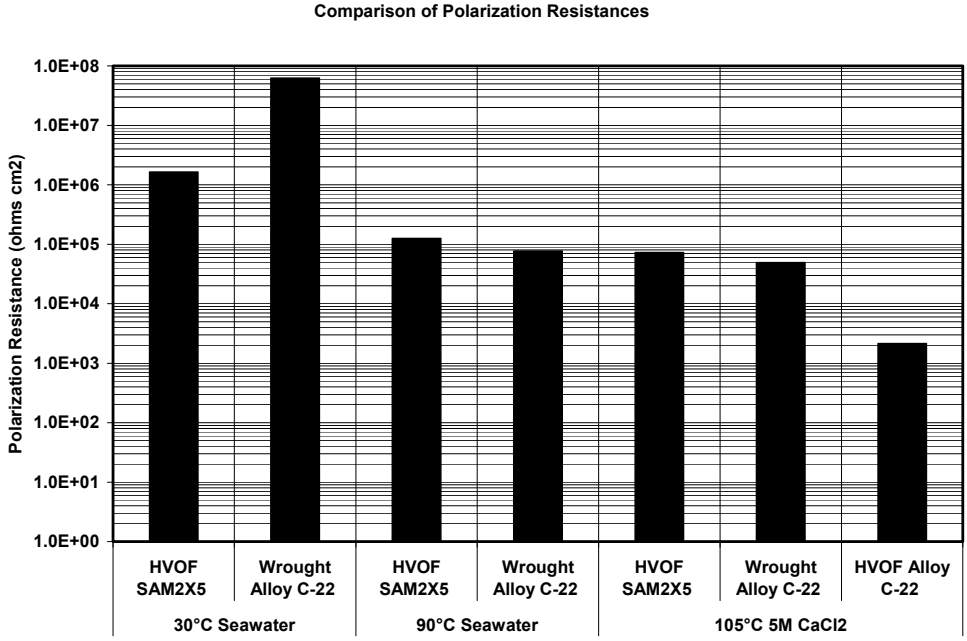

Figure 25 – Linear polarization was used to determine the polarization resistance for thermal spray coatings of SAM2X5 and the reference material (wrought nickel-based Alloy C-22) in three relevant environments, natural seawater at two temperature levels, and in hot concentrated calcium chloride (5M $CaCl_2$ at 105°C).

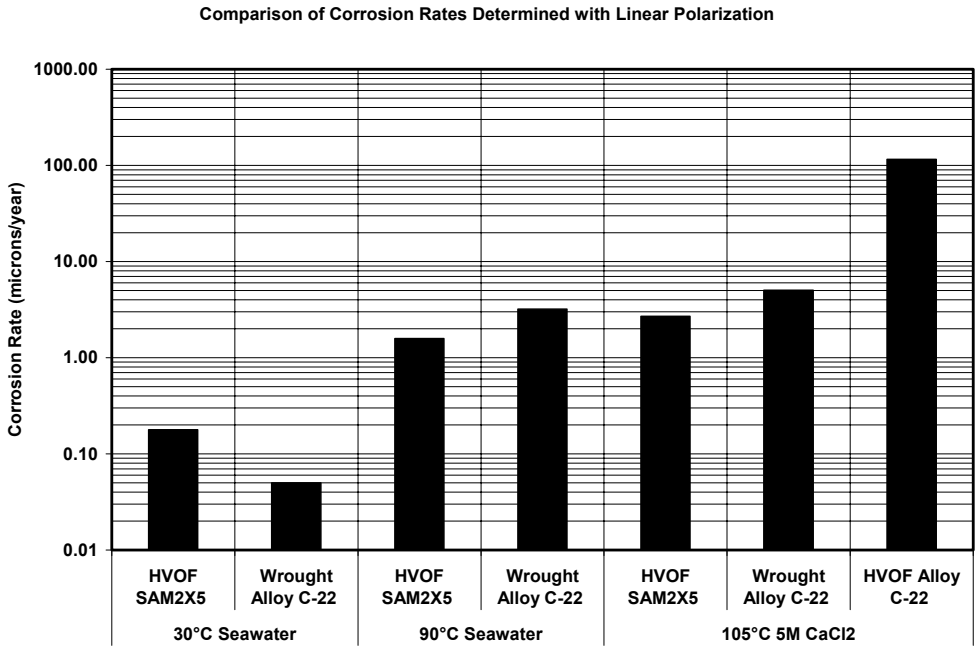

Figure 26 – Values of the polarization resistance shown in Figure 25 were converted to corrosion rates for the thermal spray coatings of SAM2X5 and the reference material (wrought nickel-based Alloy C-22) in three relevant environments, natural seawater at two temperature levels, and in hot concentrated calcium chloride (5M $CaCl_2$ at 105°C).

Type 316L Coating After Exposure for 13 Cycles

Original SAM40 (DAR40) – Corrosion After 13 Cycles

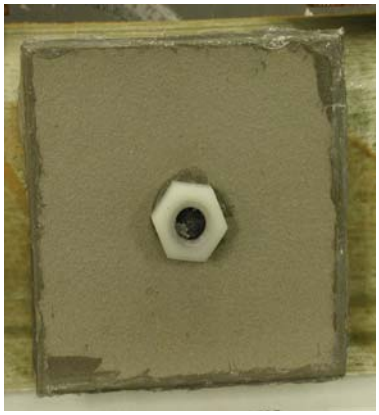

SAM2X5 – No Corrosion After 60 Cycles

Figure 27 – Salt fog testing was conducted on several thermal spray coatings, including HVOF coatings of SAM40 (also referred to as DAR40) after 13 cycles in the GM salt fog test, and amorphous SAM2X5 (also referred to as LDAR2X5) after more than 30 cycles in the GM salt fog test. After 30 cycles, the HVOF coating of Alloy C-22 showed slight rusting (not shown), while the HVOF coatings of Type 316L stainless steel and SAM40 showed substantial corrosion. In contrast, the newer SAM2X5 formulation showed no corrosion at 30 cycles. The salt fog testing of SAM2X5 was continued to almost 60 cycles with no evidence of corrosion. The corrosion of the SAM40 has been attributed to the presence of bcc ferrite and other deleterious crystalline phases.